Draft version April 14, 2021
Typeset using LaTeX **twocolumn** style in AASTeX62

The NANOGrav 12.5-Year Data Set: Polarimetry, Rotation Measures, and Galactic Magnetic Field Strengths from NANOGrav Observations with the Green Bank Telescope

H. M. Wahl,[1,2] M.A. McLaughlin,[1,2] P. A. Gentile,[1,2] M. L. Jones,[3] R. Spiewak,[4,5] Z. Arzoumanian,[6] K. Crowter,[7] P. B. Demorest,[8] M. E. DeCesar,[9,10] T. Dolch,[11,12] J. A. Ellis,[13] R. D. Ferdman,[14] E. C. Ferrara,[15] E. Fonseca,[16] N. Garver-Daniels,[1,2] G. Jones,[17] M. T. Lam,[18,19] L. Levin,[20] N. Lewandowska,[1,2] D. R. Lorimer,[1,2] R. S. Lynch,[21] D. R. Madison,[1,2] C. Ng,[22] D. J. Nice,[9] T. T. Pennucci,[23,24,*] S. M. Ransom,[23] P. Ray,[25] I. H. Stairs,[7] K. Stovall,[8] J. K. Swiggum,[9,*] and W. W. Zhu[26]

[1] *Department of Physics and Astronomy, West Virginia University, P.O. Box 6315, Morgantown, WV 26506, USA*
[2] *Center for Gravitational Waves and Cosmology, West Virginia University, Chestnut Ridge Research Building, Morgantown, WV 26505, USA*
[3] *Center for Gravitation, Cosmology and Astrophysics, Department of Physics, University of Wisconsin-Milwaukee, P.O. Box 413, Milwaukee, WI 53201, USA*
[4] *Jodrell Bank Centre for Astrophysics, Department of Physics and Astronomy, University of Manchester, Manchester M13 9PL, UK*
[5] *Centre for Astrophysics and Supercomputing, Swinburne University of Technology, P.O. Box 218, Hawthorn, Victoria 3122, Australia*
[6] *X-Ray Astrophysics Laboratory, NASA Goddard Space Flight Center, Code 662, Greenbelt, MD 20771, USA*
[7] *Department of Physics and Astronomy, University of British Columbia, 6224 Agricultural Road, Vancouver, BC V6T 1Z1, Canada*
[8] *National Radio Astronomy Observatory, 1003 Lopezville Rd., Socorro, NM 87801, USA*
[9] *Department of Physics, Lafayette College, Easton, PA 18042, USA*
[10] *AAAS, STPF, ORISE Fellow hosted by the U.S. Department of Energy*
[11] *Department of Physics, Hillsdale College, 33 E. College Street, Hillsdale, MI 49242, USA*
[12] *Eureka Scientific, Inc. 2452 Delmer Street, Suite 100, Oakland, CA 94602-3017*
[13] *Infinia ML, 202 Rigsbee Avenue, Durham NC, 27701*
[14] *School of Chemistry, University of East Anglia, Norwich, NR4 7TJ, United Kingdom*
[15] *NASA Goddard Space Flight Center, Greenbelt, MD 20771, USA*
[16] *Department of Physics, McGill University, 3600 University St., Montreal, QC H3A 2T8, Canada*
[17] *Department of Astronomy, Columbia University, 550 W. 120th St. New York, NY 10027, USA*
[18] *School of Physics and Astronomy, Rochester Institute of Technology, Rochester, NY 14623, USA*
[19] *Laboratory for Multiwavelength Astrophysics, Rochester Institute of Technology, Rochester, NY 14623, USA*
[20] *Jodrell Bank Centre for Astrophysics, School of Physics and Astronomy, The University of Manchester, Manchester M13 9PL, UK*
[21] *Green Bank Observatory, P.O. Box 2, Green Bank, WV 24944, USA*
[22] *Dunlap Institute for Astronomy and Astrophysics, University of Toronto, 50 St. George St., Toronto, ON M5S 3H4, Canada*
[23] *National Radio Astronomy Observatory, 520 Edgemont Road, Charlottesville, VA 22903, USA*
[24] *Institute of Physics, Eötvös Loránd University, Pázmány P. s. 1/A, 1117 Budapest, Hungary*
[25] *Space Science Division, Naval Research Laboratory, Washington, DC 20375-5352, USA*
[26] *National Astronomical Observatories, Chinese Academy of Science, 20A Datun Road, Chaoyang District, Beijing 100012, China*

(Received ?; Revised ?; Accepted ?)

Abstract

We present polarization profiles for 24 millisecond pulsars observed at 820 and 1500 MHz with the Green Bank Telescope by the NANOGrav pulsar timing array. We use Mueller matrix solutions calculated from observations of PSRs B1929+10 and J1022+1001 to calibrate the data. We discuss the polarization profiles, which can be used to constrain pulsar emission geometry, and also present the discovery of very low intensity average profile components ("microcomponents") in four pulsars. Using the rotation measures we measured for each pulsar, we calculate the Galactic magnetic field parallel to the line of sight for different lines of sight through the interstellar medium. We fit for linear and sinusoidal trends in time in the rotation measure, dispersion measure, and Galactic magnetic field.

Corresponding author: H.M. Wahl
hmw0023@mix.wvu.edu

We detect rotation measure variations with a period of one year in some pulsars but overall find that the variations in these parameters are more consistent with a stochastic origin.

Keywords: pulsars: general, ISM: magnetic fields, techniques: polarimetric

1. INTRODUCTION

Pulsars are highly-magnetized, rapidly-rotating neutron stars that emit electromagnetic radiation that sweeps across our line of sight as they rotate. In addition to being laboratories for study themselves, pulsars are useful in probing the properties of the interstellar medium (ISM). As the radio waves from a pulsar traverse the Galaxy, they experience Faraday rotation, which is a frequency-dependent rotation of the polarization position angle by the Galactic magnetic field. Faraday rotation changes the angle of linear polarization by an angle

$$\beta = \frac{e^3\lambda^2}{2\pi m_e^2 c^4}\int_0^d n_e(l)B_\parallel(l)dl \ , \tag{1}$$

where e is the charge of the electron, λ is the wavelength of the radio waves, m_e is the mass of the electron, c is the speed of light, n_e is the free electron density along a line of sight l, d is the pulsar distance, and $B_\parallel$ is the magnetic field parallel to the line of sight (in cgs units). The degree to which the pulsar's radio waves are rotated is called the rotation measure (RM), where

$$\mathrm{RM} = \frac{\beta}{\lambda^2} \ . \tag{2}$$

The dispersion measure (DM) is the integrated free electron density along the line of sight

$$\mathrm{DM} = \int_0^d n_e(l)dl \tag{3}$$

and varies with the observational frequency as ν^{-2}.

We can calculate the parallel component of the magnetic field along the line of sight using both the DM and RM as

$$\langle B_\parallel \rangle = 1.23\frac{\mathrm{RM}}{\mathrm{DM}}\mu\mathrm{G} \ , \tag{4}$$

where RM is in rad m^{-2} and DM is in pc cm^{-3}.

When the radio waves reach the receiver on the telescope, the telescope's response alters the components of the waves. These components can be described by the Stokes vector

$$S = \begin{bmatrix} I \\ Q \\ U \\ V \end{bmatrix} \ , \tag{5}$$

where Stokes I is the total intensity, Stokes Q and Stokes U form the linear polarization through $L = \sqrt{Q^2 + U^2}$, and Stokes V is the circular polarization intensity. Using the International Astronomical Union (IAU)'s circular polarization sign convention, right-handed circular polarization is positive (corresponding to a clockwise rotation of the position angle) and left-handed circular polarization is negative (corresponding to a counterclockwise rotation of the position angle) (Stokes 1851). The total amount of polarized emission can be described by the latter three Stokes parameters $P = \sqrt{L^2 + V^2}$.

The orientation of the linearly polarized radio waves emanating from the pulsar can be described by the position angle (PA) of the linearly polarized emission:

$$\Psi = 0.5\tan^{-1}\frac{U}{Q}.$$

The polarization angle is quoted using the IAU convention with the polarization angle increasing in the counterclockwise direction. We can solve for the telescope's response to the incoming radio waves

$$S_{\mathrm{meas}} = MS_{\mathrm{src}} \tag{6}$$

where S_{meas} is the Stokes vector measured at the telescope, S_{src} is the Stokes vector of the incoming radio waves, and M is the Mueller matrix, which depends on the ellipticity of the receiver arms, non-orthoganality of the receivers, the differential gain, and the differential phase of the receiver (see Heiles et al. 2001 for more details).

By observing a strong polarized source through a series of telescope azimuth angles, Mueller matrix elements for a given telescope and observing system can be determined. The Mueller matrix can then be used to correct other observational data and recover the intrinsic Stokes parameters of the source under observation. We can determine the Mueller matrix for a certain receiver by taking a long observation of one pulsar and tracking it across the sky. By doing this for multiple epochs, we

* NANOGrav Physics Frontiers Center Postdoctoral Fellow

can judge the stability of the receiver by observing how the solutions change over a long period of time.

Pulsars are highly-polarized sources, and the position angle can vary across the pulse phase. For many pulsars, this follows an S-shaped curve, interpreted through the rotating vector model (RVM; Radhakrishnan & Cooke 1969) as the observer's line of sight traversing a conal emission beam, with radio emission originating from the open magnetic field lines. The position angle is measured with respect to the magnetic axis such that it will rotate through the pulse by 180° at most.

Numerous polarization studies on MSPs (Kramer et al. 1998; Xilouris et al. 1998; Stairs et al. 1999) have demonstrated that most MSPs have more complex position angle curves which are notoriously difficult to fit to this model (Craig 2014a; Stairs et al. 1999; Ord et al. 2004). This is due to the recycled nature of MSPs, which results in complicated field configurations and a reduction in the magnetic field strength, resulting in much smaller period derivatives than canonical pulsars.

Millisecond pulsars also feature emission over a large portion of the profile, with more complex profiles and less profile evolution with frequency than canonical pulsars (Kramer et al. 1998). Geometric arguments imply that pulse widths should vary as as the inverse square root of the period (Rankin 1993). In addition, the beams of millisecond pulsars are wider than those of canonical pulsars due to emission that is produced farther out in the magnetosphere. This is supported by recent studies with the NICER telescope, which show that MSPs radio profiles could originate in the outer edge of the beam instead of from the core of the emission beam (Guillot et al. 2019).

Gentile et al. (2018) published fully-calibrated polarization profiles at 430 MHz, 1400 MHz, and 2300 MHz for 29 MSPs based on the NANOGrav 11-year data set (Arzoumanian et al. 2018) using the Arecibo Telescope. As expected, analysis of these profiles showed position angles that are generally inconsistent with the RVM. They also found microcomponents, which they defined as pulse components with peak intensities much lower than the total pulse peak intensity, in three pulsars.

In this paper, we present polarization profiles[1] of 24 MSPs observed with the Green Bank Telescope (GBT) at both 820 MHz and 1400 MHz as part of the NANOGrav 12.5-year data set (Alam et al. 2020).

We measure how the rotation and dispersion measures, and hence $\langle B_{\parallel} \rangle$ (i.e. from Equation 3), vary over the course of the data set.

[1] These data are available to be downloaded from data.nanograv.org/polarization.

In §2, we detail the observations. In §3 we discuss the polarimetric calibration, Faraday rotation fits, ionospheric corrections, and magnetic field calculations. In §4, we detail the results of the calibration and examine the profiles each pulsar. In §5, we discuss rotation measure, dispersion measure, and magnetic field variations, microcomponents, emission geometry, and implications for timing.

2. OBSERVATIONS

We present a subset of the NANOGrav 12.5-year data set taken between MJDs 55339 and 56739 (May 23, 2010 and March 23, 2014) at 820 MHz and 1500 MHz with the GUPPI instrument. We analyze observations of 24 pulsars, two of which overlap with Gentile et al. (2018) (PSRs J1713+0747 and B1937+21). Most pulsars were observed on a monthly cadence, with the exception of PSRs J1713+0747 and J1909−3744, which were observed weekly starting in 2013. The frequency resolution of these observations is 1.6 MHz. Table 1 shows the data timespan and number of observations for each pulsar at each frequency.

The data were run through the standard NANOGrav radio frequency interference (RFI) excision pipeline; the minimum and maximum values in the off-pulse region were found and any channels for which this value was an outlier relative to the surrounding channels were zapped (see Alam et al. 2020 for more details).

NANOGrav timing observations with the GUPPI data acquisition instrument began in 2010 March and continued into 2020. However, a technical problem arose in 2014 March, making all data collected after this date unsuitable for polarimetric work. The problem was instability in the time alignment of the digitizers for the X- and Y-polarizations of the telescope signal. This corrupted the polarization cross-products and made it impossible to recover full Stokes parameters from these data. The power in the two individual polarizations was uncorrupted, and well-calibrated total intensity measurements could still be derived, allowing for the use of these data in timing even without full Stokes parameter information.

3. DATA ANALYSIS

3.1. *Calibration Method*

All NANOGrav observations go through a basic polarization calibration procedure. At the telescope, a 25-Hz broadband signal is generated at a noise diode and injected into the receiver. At the beginning of each observation, this artificial noise signal is split into two polarization signal paths and measured with the pulsar backend.

Table 1. Number and timespan of observations for each pulsar.

	820 MHz			1500 MHz		
Pulsar	Start	End	# of Obs	Start	End	# of Obs
J0340+4130	55972	56726	30	55972	56278	30
J0613−0200	55339	56706	53	55429	56733	44
J0636+5128	56677	56727	3	56640	56729	3
J0645+5158	55828	56706	31	55826	56736	36
J0740+6620	56675	56735	3	56640	56736	4
J0931−1902	56387	56706	12	56351	56703	14
J1012+5307	55339	56706	49	55389	56431	35
J1024−0719	55339	56727	46	55364	56703	50
J1125+7819	56675	56709	3	56640	56736	6
J1455−3330	55340	56709	51	55429	56736	45
J1600−3053	55340	56675	41	55616	56733	45
J1614−2230	55340	56709	49	55265	56733	61
J1643−1224	55361	56709	47	55365	56733	52
J1713+0747	55340	56709	51	55364	56710	77
J1744−1134	55340	56735	35	55365	56736	47
J1747−4036	55976	56735	26	55977	56736	31
J1832−0836	56354	56735	16	56367	56736	16
J1909−3744	55340	56736	53	55365	56733	75
J1918−0642	55340	56735	49	55390	56733	52
B1937+21	55361	56709	46	55365	56676	40
J2010−1323	55340	56735	48	55365	56733	49
J2145−0750	55340	56709	48	55390	56736	52
J2302+4442	56003	56726	32	55972	56728	27

NOTE—These numbers reflect only the data used in the analysis;the outliers have been removed.

A calibration scan is taken for every NANOGrav observation. The noise signals themselves, and also the power in both X- and Y-polarizations, are calibrated by observations on and off a bright, unpolarized source (for the GBT, this is quasar B1442+101; NANOGrav Collaboration et al. 2015).

A set of four scans: pulsar, noise diode (which is the off-quasar scan), pulsar and noise diode, and quasar and noise diode, are used to obtain flux and polarization calibration solutions. A noise diode is observed with every pulsar scan but B1442+101 is observed once per each multi-day observing session at each frequency. This constitutes the standard calibration scheme, which is applied to all NANOGrav observations. While likely sufficient for timing purposes, in order to study the polarization in detail, more rigorous and precise polarization calibration is needed.

In this analysis, we used long-track observations of two pulsars to calculate Mueller matrix solutions. For our 820 MHz data, we used observations of PSR B1929+10 acquired by Kramer et al. (in prep.) for the double pulsar, which were shared with NANOGrav. PSR B1929+10 is known for being very bright and has well-known polarization characteristics. We solved for the Mueller matrix at six epochs (MJDs 56244, 56419, 56608, and 56793) and used the solution closest to the epoch of each pulsar observation to calibrate the 820 MHz data. The solutions produced calibrated profiles for PSR B1929+10 that matched those in the literature (e.g., Stairs et al. 1999; Dai et al. 2015; Gentile et al. 2018) for every epoch, which confirmed that our solutions accurately calibrated the data (see van Straten 2004 for full details of our calibration procedure).

At 1500 MHz, we used a single long-track observation of PSR J1022+1001 taken on MJD 55670 (2011 April 19) to calculate a Mueller matrix solution. Note that while PSR J1022+1001 has been found to show pulse profile

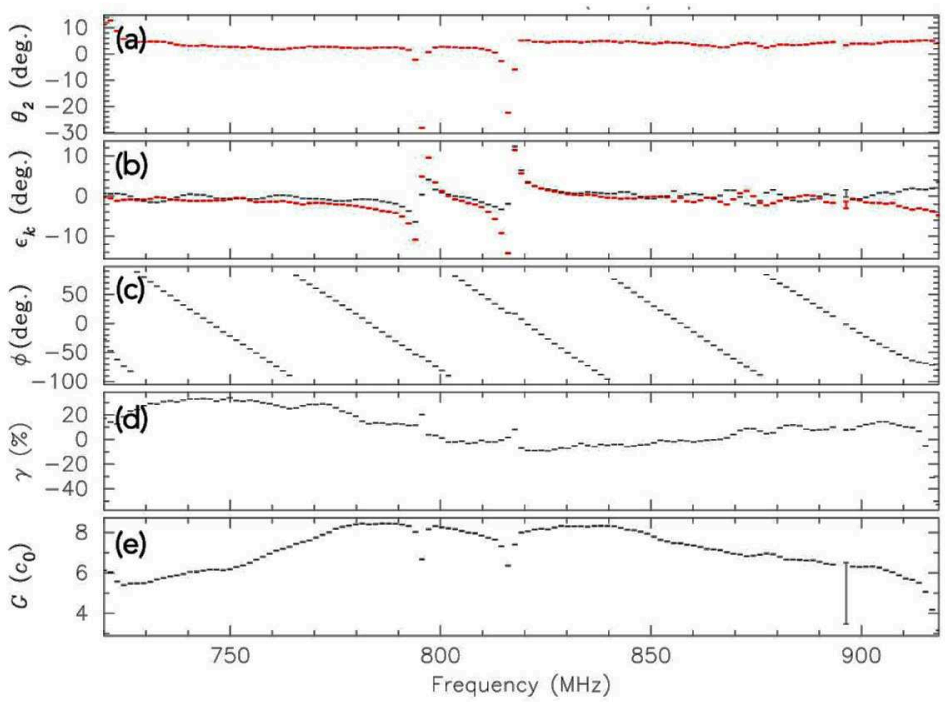

Figure 1. An example solution (MJD 56244) used to calibrate the data. Panel (a) shows the degree of cross-coupling between receivers, (b) shows the ellipticity of the receivers (the two colors show the two polarizations; θ_1 is assumed to be zero so black is not shown in the above panel.), (c) shows the differential phase, (d) shows the differential gain, and (e) shows the absolute gain of the receiver (specified in units of the square root of the reference flux density). (See van Straten 2004 for more details of this procedure).

variations by at most a few percent over the course of a year (Hotan et al. 2004), we do not expect this to affect our observations, as we observe the pulsar on a single day. After calibrating all of the data with the single solution, we found that the profiles were similar to both those in the literature (e.g., Stairs et al. 1999; Dai et al. 2015) and to each other, showing that using a single solution for multiple epochs produces accurately-calibrated profiles.

Figure 1 shows an example of an 820 MHz solution used to calibrate our data. Panel (a) shows θ, the degree of cross-coupling between the receivers. Panel (b) shows ϵ, which indicates how much Stokes Q has leaked into Stokes V. The slight leakage of one Stokes parameter into another is caused by a small amount of non-orthogonality in the receivers. Panel (c) shows ϕ, the differential phase, which quantifies the mixing of the Stokes U and V parameters. Panel (d) shows γ, the differential gain. Ideally, $\gamma = 0$; in our data set, this parameter is consistent with zero for nearly all the epochs, with only slight offsets. Finally, Panel (e) shows G, the absolute gain for the receiver. As described earlier, we measured six independent realizations of the Mueller matrix as a function of frequency at 820 MHz at six different epochs. These realizations were generally consistent with each other.

3.2. *Fitting for Faraday Rotation*

To fit for Faraday rotation, we used the *rmfit* feature of PSRCHIVE (van Straten et al. 2012), which uses a brute-force method to search for the peak of the linear polarization.

To ensure there were no outliers in RM values due to instrumental effects or miscalibration, we calculated the mean and RMS variations of the RMs for each pulsar and then removed data with RMs that were more than three standard deviations away from the mean from further analysis. After the first cut, a new mean was calculated and anything more than 3σ away from that value was cut. This process was repeated three times. Epochs with outlier RMs are not present in the combined (composite) profiles (Figures 3–14) and were not used in the variability analyses. Most outliers showed up on specific days at both frequencies (e.g., all profiles were excised on MJDs 55275, 55305, and 55337, likely because this was the start of the GUPPI observing program).

In addition to the method described above, we inspected the profiles by eye and eliminated any that looked noticeably different from the others. Criteria for this removal include incorrect handedness of the polarization, unusual variations in the profile baseline, and severe deviation from the composite profile on one epoch, all artifacts of a technical/instrumental problem with the observation.

Nearly all of the data sets that required outlier removal had less than 17% of observations removed. The exception was PSR J0740+6620, for which we excised 25% of the 820 MHz data and 33% of the 1500 MHz data; this high percentage is simply due to the small number (four and three, respectively) of total observations relative to the number of excised observations.

Though most outliers point to instrumental effects, high RMs that occur when a pulsar's line of sight passes close to the Sun may be due to a contribution from the solar magnetic field. We compared the epochs of the outliers we identified with those at which the relevant pulsar has the smallest elongation (the angle between the Sun and the pulsar). We also searched for outlier RMs at epochs at which DM peaks were detected. We find two such points for one pulsar, PSR J1614−2230, that correspond to its minimum elongation. See Section 5.1.3 for an in-depth discussion of these points.

3.3. *Ionospheric Corrections*

As the radio waves from the pulsar travel along our line of sight, they pass through the magnetic field of the Earth's ionosphere. This contributes to the measured RM and must therefore be subtracted to study trends in RM due to the pulsar's movement through the ISM. We use the IONFR (Sotomayor-Beltran et al. 2013) code, which takes publicly available GPS-derived total electron content maps, along with the most recent release of the International Geomagnetic Reference Field, and calculates the contribution of the ionosphere to the RM along the line of sight. The code takes into account the time of day of the observation, telescope location, and sky coordinates of the pulsar to get an accurate measurement for each hour of the day. We subtracted the ionospheric correction for the closest hour to the midpoint of each observation and were left with the RM due to the magnetic field of the ISM.

3.4. *Magnetic Field Calculations*

To accurately constrain magnetic fields along the line of sight to the each pulsar (see Equation 4), we need to take into account variations in DM. The NANOGrav data set includes DMX parameters, which measure how much the DM of an observation varies from some fiducial or reference DM (see Jones et al. 2017).

Table 2 shows the distance to each pulsar (calculated from parallax measurements from Alam et al. 2020), the DM (obtained from the par file for each pulsar), the average RM at each frequency (both corrected and uncorrected for the ionosphere), and the average magnetic field derived from the ionosphere-corrected RMs using Eqn. 4. The errors on the uncorrected RMs are those given by *rmfit*, and the errors on the corrected RMs are the errors given by *rmfit* and ionFR added in quadrature.

The error on the magnetic field at each epoch is the error from the RM and DM added in quadrature. The magnetic field value listed is the average over all epochs and both frequencies for each pulsar.

Figure 2 shows the value of the magnetic field of pulsars around the sky using the values from this work combined with those of Gentile et al. (2018). The results are consistent with those of Sobey et al. (2019), which uses pulsars and extragalactic sources in the northern sky to map the rotation measures, and hence the magnetic field of the galaxy. For the most part, our results also match those of Gentile et al. (2018) as well as the values of Dike et al. (2020) which uses the Long Wavelength Array to analyze polarization of pulsars below 100 MHz.

4. RESULTS

4.1. *Profiles/Individual Pulsars*

Here we present the polarization-calibrated average profiles from the method described in the previous section. Figures 3–14 show profiles for pulsars included in our descriptions. These composite profiles were made by summing the profiles from individual epochs. Table 3 shows the fractions of total power of the emission, average linear polarization, average circular polarization, and average absolute circular polarization of all pulsars in the data set at 820 MHz and 1500 MHz.

Table 4 shows all previously published profiles for these pulsars. We present the first published polarization profiles at any frequency for PSRs J0636+5128, J0645+5158, J0740+6620, J0931−1902, J1125+7819, J1614−2230, J1747−4036, J1918−0642, and J2302+4442. We also detect microcomponents for the first time in PSRs J1024−0719, J1455−3330, J1600−3053, and J2145−0750.

4.2. *J0340+4130*

4.2.1. *820 MHz*

The total intensity profile of PSR J0340+4130 at 820 MHz (see top left panel of Figure 3) has three components and features a bright central component with weak leading and trailing components. The linear polarization profile has three main components and the

Table 2. Properties of each pulsar and derived quantities. The RM values represent the average of all of the RMs at that frequency. The corrected RM is the average of all RM values with the contribution from the ionosphere removed; the error is a combination of the uncorrected RM and the ionospheric contribution. The B-field is the average of the B-field at the two frequencies.

			820 MHz		1500 MHz		
Pulsar	Distance (kpc)	DM (pc cm^{-3})	RM (rad m^{-2})	Corrected RM (rad m^{-2})	RM (rad m^{-2})	Corrected RM (rad m^{-2})	B-field (μG)
J0340+4130	1.4	49.6	56.8(3)	55.0(3)	50(3)	49(3)	1.29(3)
J0613−0200	1.1	38.8	23.1(3)	21.0(4)	18.3(6)	16.1(6)	0.59(1)
J0636+5128	1.1	11.1	1(4)	–1(3)	–5(2)	–7(1)	–0.5(2)
J0645+5158	1.2	18.2	–0.2(7)	–2.0(7)	2(2)	–0(2)	–0.07(6)
J0740+6620	0.44	15.0	–44.0(1)	–45.4(4)	–37(1)	–38(1)	–3.43(5)
J0931−1902	0.80	41.5	–97(1)	–99.6(9)	–67(19)	–80(18)	–2.5(3)
J1012+5307	0.76	9.0	4.3(3)	2.6(2)	4.1(2)	2.4(2)	0.34(2)
J1024−0719	1.3	6.5	–0.9(3)	–3.2(3)	–1.7(2)	–4.0(1)	–0.69(3)
J1125+7819	0.052	11.2	–27(2)	–28(2)	–27.6(5)	–29.3(4)	–3.16(9)
J1455−3330	13.0	13.6	12(1)	8(1)	16(1)	12(1)	0.91(7)
J1600−3053	2.0	52.3	–7.5(4)	–11.2(3)	–5.3(6)	–9.5(4)	–0.243(6)
J1614−2230	0.67	34.5	–27.4(3)	–30.5(2)	–26.1(2)	–29.1(1)	–1.062(5)
J1643−1224	1.4	62.4	–302.9(2)	–305.7(2)	–300.2(2)	–303.0(2)	–5.999(2)
J1713+0747	1.2	16.0	10.7(3)	8.7(2)	13.5(3)	11.2(3)	0.77(1)
J1744−1134	0.44	3.1	5.1(3)	2.3(2)	3.7(2)	0.7(1)	0.58(5)
J1747−4036	2.8	152.7	–28(3)	–33(3)	–47(2)	–52.4(2)	–0.34(2)
J1832−0836	2.9	28.2	39(2)	36(2)	43(2)	39(2)	1.65(5)
J1909−3744	1.1	10.4	4.2(3)	–0.1(2)	2.7(3)	–2.1(2)	–0.13(2)
J1918−0642	1.1	26.6	–58.9(6)	–61.4(5)	–54.7(3)	–57.5(3)	–2.75(1)
B1937+21	6.6	71.0	9.7(3)	7.8(3)	9.3(2)	7.2(1)	0.131(2)
J2010−1323	2.9	22.2	–2.1(6)	–4.9(5)	–4.9(5)	–8.0(5)	–0.36(2)
J2145−0750	0.63	9.0	–0.4(4)	–3.0(4)	–1.9(5)	–4.7(5)	–0.53(4)
J2302+4442	1.8	13.7	19.4(4)	17.4(4)	21.2(3)	19.3(3)	1.65(2)

Note—The uncorrected RM at each frequency is the average of all of the measurements at each frequency, while the error is the standard deviation of all of the measurements divided by the square root of the number of measurements. The corrected RM at each frequency is the average of all of the measurements after the ionospheric correction is subtracted from each day, and the error is the standard deviation of all of those corrected measurements divided by the square root of the number of measurements. The magnetic field errors are a combination of the *rmfit*, ionFR, and DMX errors.

second and third are not fully distinct. Our results are consistent with Bangale (2011). However, due to our signal-to-noise ratio (S/N) being much higher, we are able to discern an additional component in the linear polarization profile.

4.2.2. *1500 MHz*

The profile at 1500 MHz (see top right panel of Figure 3) features one main peak with two components. There is weak linear polarization, which is also split into two components, and right-circular polarization (here we define left as positive and right as negative), which has one component that lines up with the second component of the linear polarization.

4.3. *J0613−0200*

4.3.1. *820 MHz*

The 820 MHz profile (see bottom left panel of Figure 3) is very complex with five distinct components in the total intensity profile, the trailing component being brighter than the leading components. The linear polarization profile is just as complex, consisting of five components which line up with those of the total intensity. The circular polarization also has five compo-

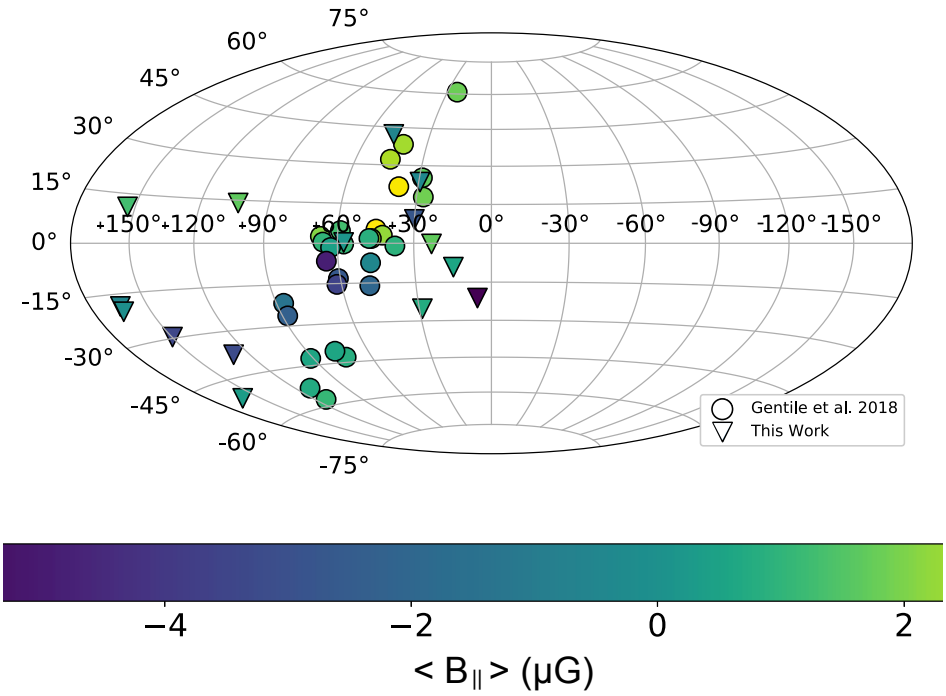

Figure 2. Magnetic field values derived from pulsar rotation measures superposed on an Aitoff plot of the Galaxy. The color bar at the bottom shows the value of $\langle B_{\parallel} \rangle$ in unit of μG. Results from this work are combined with those of Gentile et al. (2018) to get a complete picture of the values around the sky. Note: the plot of Gentile et al. (2018) is incorrect in terms of the sign of the Galactic longitude of the pulsars (which is corrected here).

nents. This profile is consistent with previous polarization profiles and position angle sweeps, such as Dai et al. (2015), at similar frequencies, the exception being that ours is right circularly-polarized and the others are left circularly-polarized, a difference purely due to the use of different sign conventions for polarization (Dai et al. 2015 uses the Institute of Electrical and Electronics Engineers definition of circular polarization whereas we use the IAU convention).

4.3.2. *1500 MHz*

The 1500 MHz profile (see bottom right panel of Figure 3) features six components that are clustered in three major peak structures. The linear polarization follows the general peak structure of the total intensity and also has six components. The profile features two components of LCP (left circularly polarization) which line up with the second and third peak structures featured in the total intensity and linear polarization.

Our profile and PA sweep are very similar to those of Dai et al. (2015) and Yan et al. (2011b) (again with the exception of a reversed circular polarization). Though the amount of circular polarization stays roughly the same from 820 MHz to 1500 MHz, the sign changes (it starts as RCP and changes to almost fully LCP).

4.4. *J0636+5128*

4.4.1. *820 MHz*

The 820 MHz profile of PSR J0636+5158 (see top left panel of Figure 4) is fairly simple, consisting of one bright component for the total intensity and linear polarization and a weak single RCP (right circular polarization) component.

4.4.2. *1500 MHz*

The 1500 MHz profile (see top right panel of Figure 4) looks almost identical to the 820 MHz profile with the exception of bifurcations of some components. A weak leading component appears on the edge of both the total intensity and the linear polarization. The single component of RCP, which before was just on the leading edge of the profile, becomes brighter and a new weak LCP component appears before turning back to RCP. Compared to 820 MHz, the pulsar exhibits a similar amount of linear polarization and more circular polarization at this frequency.

4.5. *J0645+5158*

4.5.1. *820 MHz*

This pulsar (see bottom left panel of Figure 4) has a leading weak component and a very bright main peak, which is followed by two weaker components for a total of four in the total intensity profile. The linear polar-

Table 3. Polarized intensity parameters. ⟨P⟩ is the phase-averaged power, ⟨L⟩ is the phase-averaged linear polarization, ⟨V⟩ is the phase-averaged circular polarization, ⟨V⟩ is the phase-averaged absolute value of the circular polarization, and I is the total intensity. The polarization fractions reported are those of the composite profiles.

Pulsar	⟨P⟩/I		⟨L⟩/I		⟨V⟩/I		⟨|V|⟩/I	
	820 MHz	1500 MHz	820 MHz	1500 MHz	820 MHz	1500 MHz	820 MHz	1500 MHz
J0340+4130	0.28	0.11	0.28	0.10	0.00	0.05	0.04	0.07
J0613−0200	0.09	0.19	0.07	0.19	0.05	0.00	0.03	0.04
J0636+5128	0.36	0.46	0.36	0.46	0.02	0.02	0.10	0.13
J0645+5158	0.21	0.08	0.20	0.08	0.03	0.01	0.11	0.05
J0740+6620	0.33	0.23	0.33	0.23	0.01	0.01	0.26	0.11
J0931−1902	0.20	0.32	0.20	0.32	0.01	–0.03	0.07	0.17
J1012+5307	0.66	0.53	0.66	0.53	0.02	0.03	0.04	0.08
J1024−0719	0.12	0.08	0.12	0.08	0.01	–0.01	0.03	0.02
J1125+7819	0.12	0.18	0.11	0.13	0.04	0.13	0.11	0.14
J1455−3330	0.15	0.19	0.15	0.18	0.03	0.04	0.06	0.07
J1600−3053	0.28	0.22	0.28	0.22	0.00	0.02	0.03	0.10
J1614−2230	0.05	0.63	0.05	0.63	0.00	0.00	0.02	0.04
J1643−1224	0.07	0.11	0.05	0.08	0.04	0.07	0.04	0.08
J1713+0747	0.19	0.12	0.19	0.12	0.03	0.02	0.04	0.01
J1744−1134	0.04	0.04	0.04	0.04	0.02	0.00	0.01	0.01
J1747−4036	0.08	0.09	0.08	0.09	0.00	0.02	0.02	0.03
J1832−0836	0.21	0.28	0.20	0.28	0.05	0.03	0.12	0.10
J1909−3744	0.03	0.02	0.02	0.02	0.01	0.01	0.01	0.01
J1918−0642	0.07	0.19	0.06	0.19	0.04	0.05	0.02	0.06
B1937+21	0.05	0.30	0.05	0.30	–0.01	0.00	0.01	0.02
J2010−1323	0.14	0.09	0.14	0.09	0.02	0.02	0.09	0.06
J2145−0750	0.14	0.15	0.14	0.15	–0.02	–0.01	0.09	0.07
J2302+4442	0.35	0.46	0.35	0.46	0.02	0.01	0.03	0.03

ization profile contains six weak components which generally follow the shape of the total intensity (the peaks line up with the three total intensity components). The circular polarization features a sharp reversal from LCP to RCP in line with the main peak of the total intensity, then three weak RCP components which match up with the trailing components of the total intensity. The profile features a postcursor which has one component that is weakly linearly polarized with no circular polarization.

4.5.2. *1500 MHz*

The 1500 MHz profile of PSR J0645+5158 (see bottom right panel of Figure 4) also features many complex components. The shape of the main pulse is the same as at 820 MHz, but with the trailing two components appearing brighter in proportion to the main peak. The linear polarization profile now has four distinct components, with the second and fourth being the brightest. The circular polarization is generally the same shape as at 820 MHz. Compared to our 820 MHz profile, it has a higher degree of linear polarization and is less circularly polarized. The shape of the postcursor also stays the same, with the linear polarization coming later in the profile.

4.6. *J0740+6620*

4.6.1. *820 MHz*

The 820 MHz profile (see top left panel of Figure 5) has a fairly low S/N. Two major structures, the first featuring a weak trailing and a strong leading component, and the other showing one main peak split into bright two components, are visible. Some linear polarization is seen in the first structure and some LCP is present in the second, but most of the linear and circular polarization information is lost due to noise.

4.6.2. *1500 MHz*

The 1500 MHz profile (see top right panel of Figure 5) is fairly complex. The first structure contains four

Table 4. Previously published polarization profiles.

Pulsar	Published Polarization Profiles
J0340+4130	820 MHz[(1)]
J0613−0200	410 MHz[(2)], 610 MHz[(2)], 728 MHz[(3)], 1335 MHz[(4)], 1369 MHz[(3)], 1369 MHz[(5)], 1405 MHz[(6)], 3100 MHz[(3)]
J0636+5128	—
J0645+5158	—
J0740+6620	—
J0931−1902	—†
J1012+5307	149 MHz[(7)], 610 MHz[(2)]
J1024−0719	728 MHz[(3)], 1369 MHz[(3)], 1369 MHz[(5)], 1373 MHz[(6)], 3100 MHz[(3)]
J1125+7819	—
J1455−3330	1300 MHz[(6)]
J1600−3053	728 MHz[(3)], 1369 MHz[(3)], 1369 MHz[(5)], 1373 MHz[(6)], 3100 MHz[(3)]
J1614−2230	—†
J1643−1224	610 MHz[(2)], 728 MHz[(3)], 1331 MHz[(4)], 1369 MHz[(3)], 1369 MHz[(5)], 3100 MHz[(3)]
J1713+0747	410 MHz, 610 MHz[(2)], 728 MHz[(3)], 1369 MHz[(3)], 1369 MHz[(5)], 1400 MHz[(8)], 1405 MHz[(6)], 1414 MHz[(2)], 2100 MHz[(8)], 3100 MHz[(3)]
J1744−1134	610 MHz[(2)], 728 MHz[(3)], 1341 MHz[(6)], 1369 MHz[(3)], 1369 MHz[(5)], 3100 MHz[(3)]
J1747−4036	—†
J1832−0836	728 MHz[(3)], 1369 MHz[(3)], 1369 MHz[(9)], 3100 MHz[(3)]
J1909−3744	728 MHz[(5)], 1369 MHz[(3)], 1369 MHz[(5)], 1373 MHz[(6)], 3100 MHz[(3)]
J1918−0642	—†
B1937+21	610 MHz[(2)], 728 MHz[(3)], 1369 MHz[(3)], 1369 MHz[(5)], 1373 MHz[(6)], 1400 MHz[(8)], 1414 MHz[(2)], 2100 MHz[(8)], 3100 MHz[(3)]
J2010−1323	1373 MHz[(6)]
J2145−0750	410 MHz[(2)], 610 MHz[(2)], 728 MHz[(3)], 1335 MHz[(4)], 1369 MHz[(3)], 1369 MHz[(5)], 1373 MHz[(6)], 1414 MHz[(2)], 3100 MHz[(3)]
J2302+4442	—

NOTE—References: [(1)]Bangale (2011), [(2)]Stairs et al. (1999), [(3)]Dai et al. (2015), [(4)]Manchester & Han (2004), [(5)]Yan et al. (2011b), [(6)]Ord et al. (2004), [(7)]Noutsos et al. (2015), [(8)]Gentile et al. (2018), [(9)]Burgay et al. (2013). Note: several pulsars with no previously published polarization profiles are included in a study of MeerKAT data (Spiewak et al. in prep.); these are denoted with a †.

peaks in the total intensity, four in the linear polarization (the middle two corresponding to the strongest total intensity peak), and two fully separate RCP components that also correspond to the strongest total intensity peak. The second structure contains two peaks, the trailing brighter than the leading; the linear polarization contains one weak component and the circular polarization has a weak RCP component followed by a sharp reversal to LCP.

4.7. *J0931−1902*

4.7.1. *820 MHz*

The 820 MHz profile of PSR J0931–1902 (see bottom left panel of Figure 5) has three separate structures in its pulse profile at 820 MHz. The first structure has a single peak with two weaker leading components, a linear polarization profile that contains a weak leading component and a main peak (which is split into three components) that is half as bright of the total intensity but also peaks around the same phase, and a weak LCP profile. The second structure is weak and is almost totally linearly polarized. The third structure is weaker than the first but brighter than the second and is also almost fully linearly polarized with no circular polarization.

4.7.2. *1500 MHz*

The 1500 MHz profile (see bottom right panel of Figure 5) shows some evolution from the 820 MHz profile: the leading peak on the total intensity becomes comparable to the main bright peak and the profile is more linearly polarized, and traces amount of circular polarization are detected. The second structure features two components comparable in intensity and now is almost fully unpolarized. The third structure, which has two strong components and a weak trailing component, is now nearly as intense as the first structure, and is almost fully linearly polarized (the liner polarization also being split into two components) with a weak LCP component that lines up with the brightest peak of the total intensity.

4.8. *J1012+5307*

4.8.1. *820 MHz*

The 820 MHz profile (see top left panel of Figure 6) is very complex, featuring two main structures. The first structure has two leading components followed by five bright components; the linear polarization has seven components which get brighter over the course of the profile, and there is a weak amount of circular polarization, which switches from LCP to RCP over the course of the profile. The second structure contains two distinct, comparable-intensity components and are fully linearly polarized. Those components are connected to another set of three total intensity peaks (also almost fully linearly polarized). The second structure contains no circular polarization.

4.8.2. *1500 MHz*

There is quite a bit of evolution from 820 MHz to 1500 MHz (see top right panel of Figure 6) for this pulsar. The first major structure now only has four components, as the two leading components become brighter and other components merge together; some of the components in the linear polarization merge, resulting in three major peaks, while the circular polarization stays the same shape but the components become brighter. The first part of the second structure becomes more comparable in intensity to the first structure, still featuring two distinct components but is now less linearly polarized. The second part of the second structure is still connected to the first by bridge emission and is totally linearly polarized but the polarization position angle points to a separation of the structures. At 820 MHz, there was one polarization position angle sweep that spanned the two structures but now it is separate. There is now weak LCP in the first part of the structure but still none toward the end of the structure.

4.9. *J1024−0719*

4.9.1. *820 MHz*

The 820 MHz profile of PSR J1024−0719 is very complex (see central left panel of Figure 6); the total intensity profile has six components with a weak seventh, and the first three components are almost fully linearly polarized. The linear polarization profile has eight components, the brightest components lining up with the first three of the total intensity profile and the rest being much weaker at the second half of the profile. There is a weak RCP that features three weak components. The circular polarization profile now features one LCP component which switches handedness in the center of the profile and becomes three very weak RCP components.

A very weak microcomponent with a maximum flux density of about 0.5 mJy is seen at a phase of 0.2 in our plots (see bottom left panel in Figure 6) and some linear polarization is detected. This is the first time a microcomponent in this pulsar has been detected.

4.9.2. *1500 MHz*

The overall shape of the 1500 MHz profile (see central right panel of Figure 6) is generally the same as at 820 MHz with many components, though fewer components are seen in the linear polarization profile and more are present in the circular polarization profile. The microcomponent is still visible and has a peak flux density of 0.3 mJy at this frequency (see bottom right panel in Figure 6) . Our results are consistent with those of Dai et al. (2015) and Yan et al. (2011b).

4.10. *J1125+7819*

4.10.1. *820 MHz*

The 820 MHz profile of this pulsar (see top left panel of Figure 7) shows a fairly simple peaked structure. The total intensity profile features one peak with a hint of another leading peak, and the linear polarization contains two, the brightest being more than half the that of total intensity and the second component about half of the first. There is a weak RCP component that changes to LCP, and the brightness becomes comparable to that of the weaker component of the linear polarization profile.

4.10.2. *1500 MHz*

The 1500 MHz profile of PSR J1125+7819 (see top right panel of Figure 7) shows evolution from the 820 MHz profile, mostly in the intensity of the linear polarization. Both peaks of the total intensity bifurcate, creating four components of comparable intensity. The leading components of the linear polarization become brighter and totally polarizes the first component of the total intensity, and the second peak get weaker. The shape of the circular polarization is very similar but the amplitude of the RCP and LCP component increases slightly.

4.11. *J1455−3330*

4.11.1. *820 MHz*

The high S/N of this profile allows us to see the complex structures in the 820 MHz profile of this pulsar (see center left panel of Figure 7). The total intensity profile has four components while the linear polarization is fairly weak but has six components and the weak RCP has five (two weak leading components and three stronger trailing).

After the main pulse, we detect a weak microcomponent that peaks around a phase of 0.9 in our plot (see bottom left panel of 7). It is just above the noise but is seen to be largely linearly polarized with traces of circular polarization. This is the first time this microcomponent has been detected.

4.11.2. *1500 MHz*

As we go from 820 MHz to 1500 MHz (see central right panel of Figure 7) for this pulsar, the first component of the profile weakens, the second two peaks merge into one, and the main peak absorbs the fourth peek. The linear polarization profile now only has three peaks while circular features two LCP components followed by an RCP component that is comparable in intensity to the linear polarization. Our results are consistent with those or Ord et al. (2004).

In the microcomponent (see bottom right panel of Figure 7), we can now see two peaks, the first being almost fully linearly polarized and the second being weakly linearly polarized with no circular polarization.

4.12. *J1600−3053*

4.12.1. *820 MHz*

The total intensity profile of PSR J1600−3053 at 820 MHz (see top left panel of Figure 8) shows two main components, the leading about half as bright as the trailing. The linear polarization profile has three components, the trailing component being the strongest and the central component being the weakest of the three. There is a weak LCP profile. These results are identical to those seen by Dai et al. (2015) at 728 MHz.

At a phase of around 0.2 in our plot, a microcomponent with a maximum flux density of 0.5 mJy is detected but the polarization is too noisy to make any definite statements (see central left panel of Figure 8). This is the first detection of this microcomponent.

4.12.2. *1500 MHz*

For the most part, the 1500 MHz total intensity profile (see top right panel of Figure 8) matches the 820 MHz profile. The linear polarization profile changes slightly; the central component becomes brighter than the leading and lagging components and bifurcates. There is a bit more circular polarization detected, though it is still fairly weak, and it shifts from RCP to LCP. The results identical to those of Dai et al. (2015) and Yan et al. (2011b), with the exception of the sign of circular polarization.

The microcomponent also present at this frequency (see bottom central right of Figure 8) but is barely above the noise.

4.13. *J1614−2230*

4.13.1. *820 MHz*

The 820 MHz profile of PSR J1614−2230 (see bottom left panel of Figure 8) has a weak structure containing three weak components that precede the main profile, and only weak linear polarization is detected. The main profile itself has two components, the trailing about half as bright as the main component. It is almost fully linearly polarized and there is a weak amount of LCP that lines up with the main peak of the total intensity/linear polarization.

4.13.2. *1500 MHz*

The preceding structure at 1500 MHz (see bottom right panel of Figure 8) has six components in its total intensity profile, the second half containing being partially linearly polarized. The main profile of this pulsar features a main peak that is very nearly fully polarized with some LCP.

4.14. *J1643−1224*

4.14.1. *820 MHz*

The total intensity of PSR J1643−1224 at 820 MHz (see top left panel of Figure 9) contains one main component that sharply peaks with a weak leading component. The linear polarization profile features three components, the leading being about twice as bright as the two trailing; the circular polarization starts off with RCP and switches to weak LCP halfway through the profile and becomes comparable in brightness to the linear polarization. Our results are consistent with the 720 MHz profile from Dai et al. (2015) with the exception of the different sign of circular polarization.

4.14.2. *1500 MHz*

The main profile at 1500 MHz (see top right panel of Figure 9) shows a middle component that develops on the leading edge of the main peak. The polarization shows quite a bit of evolution from 820 MHz: the second component of the linear polarization becomes more brighter than the first and the circular develops a central LCP component. Our results match those of Manchester & Han (2004), Yan et al. (2011b), and Dai et al. (2015) with the exception of the sign of the circular polarization.

4.15. *J1713+0747*

4.15.1. *820 MHz*

The total intensity profile of this pulsar at 820 MHz (see central left panel of Figure 9) has three components: a bright central component with one leading component

and two trailing components. The two weaker components of the total intensity are fully linearly polarized and the linear polarization profile itself features a total of five components . There is weak circular polarization that switches from LCP to RCP in the middle. Our profile is similar to that of Dai et al. (2015). It is also matches that of Gentile et al. (2018)'s profile, which was polarization calibrated using a different technique using Arecibo data (see §3.1 for details). Because of the high S/N of our observations, we detect the polarization angle in much higher detail and observe an RVM-like swing. We do not detect a microcomponent at this frequency.

4.15.2. *1500 MHz*

The profile of PSR J1713+0747 at 1500 MHz (see central right panel of Figure 9) is very similar to that at 820 MHz; the total intensity components are just as bright, and a new component presents itself on the leading edge of the main peak. The trailing component gets weaker, as does the second component of the linear polarization. The first component of the average profile is still fully linearly polarized and there is less circular polarization.

The polarization profile of PSR J1713+0747 has been studied by many, including Dai et al. (2015) Gentile et al. (2018), and many more, and our results are consistent with all other published profiles. Because of the high S/N of our observations, we detect the polarization angle in much higher detail and observe an RVM-like swing.

We observe a microcomponent with a maximum flux density of 0.3 mJy that peaks at a phase of 0.82 in our plot (see bottom right panel of Figure 9). The profile features some linear polarization on the trailing edge of its first peak and has no detectable circular polarization. There was no detection of this microcomponent at 820 MHz, which is likely due to the fact that the S/N of the 1500 MHz profile is three times greater than that of the 820 MHz profile, making it easier to see the microcomponent at the former frequency. Dai et al. (2015) Gentile et al. (2018), and Dolch et al. (2014) also detect this microcomponent at 1500 MHz.

4.16. *J1744−1134*

4.16.1. *820 MHz*

The main pulse of the 820 MHz profile (see top left panel of Figure 10) shows two bright components in the total intensity, the leading being much brighter than the trailing. The profile is almost fully linearly polarized and no circular polarization is detected. This pulsar has a precursor, which is also detected by Dai et al. (2015) at 728 MHz. The precursor has three components in its total intensity and some linear polarization. Kramer et al. (1998) detects a small postcursor that follows the main pulse by about 0.2 in phase and is half the intensity of the microcomponent. Neither we nor Yan et al. (2011a) detects this feature.

4.16.2. *1500 MHz*

The 1500 MHz profile of PSR J1744−1134 (see top right panel of Figure 10) features a fully linearly-polarized main component. The trailing component on the main component is now barely detectable. Our results are consistent with Dai et al. (2015), the only difference between the two works is the sign of the circular polarization. The precursor, also identified by Dai et al. (2015), is very similar to that at 820 MHz, the only difference being a slightly weaker linear polarization.

4.17. *J1747−4036*

4.17.1. *820 MHz*

At 820 MHz (see bottom left panel of Figure 10), the total intensity profile is very wide and has two bright components with two weaker components on either side of the second peak, which are all very weakly linearly polarized. There is a very weak RCP component that lines up with the first bright peak of the total intensity.

4.17.2. *1500 MHz*

At 1500 MHz (see bottom right panel of Figure 10), the leading component is much brighter than the lagging and there is almost no emission between the components. The two weaker components merge with the second component in the total intensity profile. The linear and circular polarization (RCP) profiles peak at the same phase as the leading total intensity component though are only about a quarter the brightness of the total intensity. The second component in the total intensity profile is much broader than the leading component and has weak linear polarization with traces of circular polarization.

4.18. *J1832−0836*

4.18.1. *820 MHz*

The profile of PSR J1832−0836 at has three major structures at 820 MHz (see top left panel of Figure 11), the first featuring two peaks in total intensity, the major one being the trailing component. There are two weak components in the linear polarization and an even weaker LCP component. The second structure contains two separate peaks, both have equal linear and RCP. The last structure is weak compared to the others and is almost fully linearly polarized with no circular polarization.

4.18.2. *1500 MHz*

The 1500 MHz profile (see top right panel of Figure 11) contains similar structures to the 820 MHz profile. The peaks on the first structure have separated and are now distinct, the first peak being fully linearly polarized and the other peak having a linear polarization component that peaks at the same phase. The second structure now contains two bright components and a third weaker component. The linear polarization profile of the second structure also has two peaks which are equal in intensity. The RCP profile has the same amount of peaks. The third structure is again totally linearly polarized and has a weak LCP. The profile and PA sweep are consistent with Burgay et al. (2013)'s 1369 MHz observation of this pulsar as well as Dai et al. (2015)'s.

4.19. *J1909−3744*

4.19.1. *820 MHz*

At 820 MHz (see central left panel of Figure 11), the main peak of this profile is very bright in its total intensity while the the linear polarization is half as bright and contains two components. The LCP is about half as bright as the linear and mirrors the structure of the linear polarization profile. The profile and PA sweep are consistent with Dai et al. (2015)'s observations at 728 MHz.

We detect a microcomponent that has a peak at 2 mJy that has two components (see bottom left panel in Figure 11). The second component is weakly linearly polarized with traces of circular polarization. This microcomponent was previously noted in the work of Dai et al. (2015).

4.19.2. *1500 MHz*

The only major change between 820 MHz and 1500 MHz (see third row on the right panel of Figure 11) in is that lagging component of both the linear and circular polarization becomes a bit brighter than the leading component. Our results are consistent with those of Yan et al. (2011b) with the exception of the sign of the circular polarization.

The microcomponent retains its structure at this frequency, though the linear polarization is now barely detectable (see bottom right panel in Figure 11).

4.20. *J1918−0642*

4.20.1. *820 MHz*

The total intensity profile at 820 MHz (see top left panel of Figure 12) contains one central bright peak and three leading components and two trailing. The linear polarization profile also features one bright peak (about half as bright as the total intensity peak) and two more trailing components. The circular polarization is about half the power of the linear and peaks at the same phase after changing from LCP to RCP. A weakly linearly polarized precursor with no circular polarization is also present.

4.20.2. *1500 MHz*

The main difference between the profile at 1500 MHz (see top right panel of Figure 12) and 820 MHz is the leading components on the average profile: the first profile component gets brighter relative to the main profile and separates from the main component. The shape of the precursor total intensity and polarization profiles stays the same with the exception of the disappearance of one of the weaker central components of the linear polarization.

4.21. *B1937+21*

4.21.1. *820 MHz*

The 820 MHz profile of PSR B1937+21 (see central left panel of Figure 12) shows two main structures. The first structure shows a bright single peak which is highly linearly polarized, and has a detectable amount of LCP that has its peak aligned with that of the total intensity and linear polarization peaks. The second structure is about half as bright and is weakly polarized, the linear polarization profile consisting of three components below 100 mJy and the LCP barely detectable. This profile matches that of Dai et al. (2015), though the components of the linear polarization on the second structure are less well-defined.

Between the two pulses, we detect a microcomponent at an intensity of 3 mJy (see bottom left panel of Figure 12. This microcomponent is fully linearly-polarized and were detected by Dai et al. (2015).

At 820 MHz, B1937+21 showed variability mostly in the degree of linear polarization in the second main structure (the interpulse). Because the RMs matched published values, we chose to carry out the analysis with them; the average profile is also similar to the literature, so we chose to present it. Because the variability appears in the polarization and not total intensity, we attribute it to a calibration error and will explore it in future work.

4.21.2. *1500 MHz*

The 1500 MHz (see central right panel of Figure 12) first structure has two components, the leading much brighter than the lagging. The linear polarization profile shows three components; a weak leading component is followed by a bright central component and a trailing component that is half as bright as the main component. Very little LCP is detected. The second structure also

contains two components in its total intensity profile, though the second is very weak compared to the leading. The linear polarization profile has one weak component with a trace of a second component and barely any circular polarization. The linear polarization in the main component of B1937+21 at 1500 MHz is comparable to that at 820 MHz, as is the circular polarization. Because of the high S/N of our observations, we detect the polarization angle in much higher detail than previous works.

The polarization profile of PSR B1937+21 has been studied extensively at L-band (for example, Stairs et al. (1999) and Dai et al. (2015)) and our results are generally consistent with the literature. The polarization profiles are generally in agreement as well, though the number of components on the linear polarization profile of the main pulse and the intensity of them is different; Stairs et al. (1999)) detect one bright component and two weak components, while Dai et al. (2015) detect a bright component and one weak component, and we detect two components of comparable intensity. The profile we present is similar to Gentile et al. (2018)'s profile with the exception of the intensity of the second component on the main pulse, but is most similar to that of Dai et al. (2015). This discrepancy between the intensity of the second component of the profiles is due to the fact that that component is known to vary on the timescales of about a year (Brook et al. 2018).

The microcomponent between the two pulses has two components in itself, one having a flux density of 1 mJy and the other about half its size (see bottom right panel of 12). Some linear polarization is detected but very little, if any, circular polarization is detected. These components have been detected by Gentile et al. (2018) and Dai et al. (2015).

4.22. *J2010−1323*

4.22.1. *820 MHz*

The 820 MHz total intensity profile (see top left panel of Figure 13) features a bright peak with a trailing component connected to the first. The linear polarization is fairly weak and has two components, the second much wider than the first. The LCP is as bright as the linear polarization and peaks around the phase of second component of the linear polarization profile. The circular polarization later switches to RCP and peaks slightly before leveling off. Our profile is similar to that of Ord et al. (2004), though ours has a much higher S/N which allows us to resolve the polarization in higher detail.

4.22.2. *1500 MHz*

The shape of the profiles at 1500 MHz (see top right panel of Figure 13) is very similar to the shape at 820 MHz, the main difference being that the linear polarization becomes brighter in comparison to the main peak. The trailing component of the total intensity also separates slightly from the main component.

4.23. *J2145−0750*

4.23.1. *820 MHz*

The 820 MHz profile of the pulsar (see central left panel of Figure 13) features multiple components and a precursor. At this frequency, the precursor is fully linearly polarized. The main total intensity peak features one bright peak followed be three components after a bridge component. The linear polarization contains two peaks of equal intensity followed by a dip and then two more, while the circular polarization profile contains a fairly bright LCP peak, goes to zero, and then switches to a RCP peak comparable in intensity to the LCP peak. It is consistent with that of Dai et al. (2015). We see a highly linearly-polarized precursor to the main profile, which is also seen by Dai et al. (2015).

We also detect a microcomponent after the pulse profile with a maximum amplitude of 1.4 mJy (see bottom left panel of Figure 13, which is highly linearly-polarized and has a circular polarization equal to its amplitude but opposite to its sign. This is the first time this component has been detected.

4.23.2. *1500 MHz*

The 1500 MHz profile (see central right panel of Figure 14) is equally as complex as the 820 MHz profile. A central component in the bridge emission arises while the trailing components weaken. The structure of the polarization profiles stay the same with the exception of the first component of the linear polarization profile growing weaker than the others. The polarization profile and PA sweep match those presented in many past works, including Dai et al. (2015) and Manchester & Han (2004). The precursor also stays the same, and this matches observations of Dai et al. (2015)

The microcomponent is visible with a maximum flux density of 0.3 mJy (see bottom right panel of Figure 13; it has very weak linear polarization and the circular polarization, again, is comparable to the total intensity of the microcomponent found by Dai et al. (2015) but is the opposite sign.

4.24. *J2302+4442*

4.24.1. *820 MHz*

The 820 MHz profile of this pulsar (see left panel of Figure 14) is very wide, spanning almost the entire phase range. The total intensity of the 820 MHz profile contains three major structures: the first structure

has three components is totally linearly polarized, the second contains two components in which the linear polarization is slightly weaker, and a third structure has five components and is slightly linearly polarized by a two-component linear polarization profile. Very little circular polarization is present in the profile.

4.24.2. *1500 MHz*

The 1500 MHz pulse profile (see right panel of Figure 14) is equally as complex as it was at 820 MHz. The first structure, which features five components, is fully linearly polarized. The second structure features contains three components, with the linear polarization containing two. There is then a bridge component before the third structure where the linear polarization weakens and then increases to become two separate components in the third structure. There is very weak circular polarization detected.

5. DISCUSSION

5.1. *Variations in Measured Values*

For each of the three parameters (ionosphere-corrected RM, DM, and $\langle B_{\parallel} \rangle$), we performed a least-squares fit weighted by the errors for a purely linear trend, a purely sinusoidal trend, and a combination of the two for all pulsars for which we have greater than one year of data. We only performed a sinusoidal and combination fit if a significant period with a false alarm probability (FAP) less than 5% was first identified through a Lomb-Scargle periodogram analysis. This FAP was calculated using the formula from Scargle (1982), which uses the length of the dataset and power spectral density to determine the probability that the period of the Lomb-Scargle periodogram is detected by random chance. That period was then used as the initial guess for the fitting. The reduced χ^2_r values were calculated for each fit; the trend reported for each pulsar is the model with the smallest reduced χ^2 value.

The parameters for the trends are reported in Tables 5–7 and the data containing the best fit trend lines are shown in Figures 15–23. We plot the two frequencies separately because the trends could look different due to systematics. In addition, one frequency may be more sensitive than another due to the pulsar's spectrum, DM, or RFI, so we may only see the trend significantly in one plot.

5.1.1. *RM Variations*

Ionosphere-corrected rotation measure variations for each pulsar are shown in the top panels of Figures 15–23 and the best-fit trends are shown in Table 5. We find that six pulsars (PSRs J1024−0719, J1643−1224, J1713+0747, J1909−3744, J1918−0642, B1937+21) show significant trends in their rotation measure values. The majority of these pulsars show a trend that is both linear and sinusoidal in nature. Two pulsars that show a sinusoidal trend have a period consistent with one year but others have a period consistent with one to two years. Because we only see two to three full periods in the data set, these trends are likely due to stochastic processes and are not true periodicities. The linear trends may also be part of a longer-timescale stochastic variation or they could be produced by a change in distance between the Earth and the pulsar, which would cause an increase or decrease in the magnetic field and electron density along the line of sight. The trends that are left unexplained can most likely be explained by these stochastic variations similar to those we see in NANOGrav's DM time series (Jones et al. 2017). See Rickett (1990) for more details on these variations in the interstellar medium.

Of the six pulsars for which we find significant trends in RM, four have detectable trends at only one frequency. We attribute these differences to smaller errors bars on RM measurements at one of the two frequencies. For PSR J1713+0747 and J1909−3744, trends are detected at both 820 and 1500 MHz, but the fits are inconsistent. This suggests that the fitted trends may not indicate true magnetic-field variations but are due to some other systematic effects.

Yan et al. (2011a) observed 20 MSPs at 2–3 week intervals for 4.8 years, measured the position angle changes over time to obtain RM variations, and averaged their measurements over 100-day intervals. There is an overlap of nine pulsars between the data sets: PSRs J0613–0200, J1024–0719, J1600–3053, J1643–1224, J1713+0747, J1744–1134, J1909–3744, B1937+21 (J1939+2134), and J2145–0750. Yan et al. (2011a) fit only for linear trends in their data and find significant RM trends in five (PSRs J0613−0200, J1643−1224, J1909−3744, B1937+21, and J2145−0750). We find no trends in J0613−0200 or J2145−0750, a purely sinusodial trend in the RM values of B1937+21, and linear + sinosiudal fit for J1643−1224 and J1909−3744, both of which have a slope that is an order of magnitude greater than that found by Yan et al. (2011a) and not within their error bars.

There is only an overlap of roughly six months between our two data sets, which may cause some differences. The averaging used by Yan et al. (2011a) over 100-day windows makes them more sensitive to long-term variations but less sensitive to daily and annual variations. They obtain their rotation measures in a slightly different way, using an iterative differential PA

Table 5. Rotation measure trends. The results of fitting a linear trend, a purely sinusoidal, and a sinusoidal + linear trend to the magnetic fields. A weighted least-squares fitting routine was performed and the periods of the sinusoidal fits are result of doing a Lomb-Scargle periodogram. Any period that had less than a 5% false alarm probability was not considered significant. Trend reported is the one with the smallest χ^2_r value.

Pulsar	Frequency (MHz)	Trend	dRM/dt (10^{-3} rad m^{-2} yr^{-1})	Amplitude (rad m^{-2})	Period (days)	χ^2_r	Pre-Fit χ^2_r	Period FAP
J1024−0719	1500	Linear	1.3(3)	—	—	3.6	5.4	—
J1643−1224	1500	Both	0.8(3)	1.0(1)	373(9)	3.1	6.2	0.6%
J1713+0747	820	Both	1.2(5)	1.5(3)	644(24)	24.6	49.0	0.1%
J1713+0747	1500	Linear	–3.3(6)	—	—	73.2	100	—
J1909−3744	820	Both	0.8(6)	1.3(3)	630(37)	9.3	12.4	3.5%
J1909−3744	1500	Both	2.0(4)	1.3(3)	387(11)	6.26	10.2	0.42%
J1918−0642	820	Both	4.2(9)	3.2(5)	601(21)	38.4	101	0.7%
B1937+21	820	Sine	—	1.5(3)	368(11)	78.7	109	4.4%

Table 6. Dispersion measure trends. The results of fitting a linear trend, a purely sinusoidal, and a sinusoidal + linear trend to the magnetic fields. A weighted least-squares fitting routine was performed and the periods of the sinusoidal fits are result of doing a Lomb-Scargle periodogram. Any period that had less than a 5% false alarm probability was not considered significant. Trend reported is the one with the smallest χ^2_r value.

Pulsar	Trend (MHz)	dDM/dt	Amplitude (10^{-4} pc cm^{-3} yr^{-1})	Period (pc cm^{-3})	χ^2_r (days)	Pre-Fit χ^2_r	Period FAP
J1012+5307	Both	0.4(2)	1.6(2)	874(51)	0.8	1.6	0.7%
J1713+0747	Both	–0.38(5)	0.61(7)	366(7)	3.1	6.7	0.3%
J1744−1134	Both	0.2(1)	0.9(2)	425(16)	3.1	4.5	0.9%
J1909−3744	Both	$-5.3(2) \times 10^{-4}$	$4(1) \times 10^{-5}$	568(46)	33.7	431	1.8%
J2302+4442	Linear	–3.5(7)	—	—	—	2.5	—

Table 7. Magnetic field trends. The results of fitting a linear trend, a purely sinusoidal, and a sinusoidal + linear trend to the magnetic fields. A weighted least-squares fitting routine was performed and the periods of the sinusoidal fits are result of doing a Lomb-Scargle periodogram. Any period that had less than a 5% false alarm probability was not considered significant. Trend reported is the one with the smallest χ^2_r value.

Pulsar	Frequency (MHz)	Trend	dB/dt (10^{-3} μG yr^{-1})	Amplitude (μG)	Period (days)	χ^2_r	Pre-Fit χ^2_r	Period FAP
J1643−1224	1500	Both	0.016(5)	0.019(3)	373(9)	3.1	6.2	0.6%
J1713+0747	820	Both	0.09(4)	0.11(2)	644(24)	24.6	49.0	0.1%
J1713+0747	1500	Linear	–0.25(5)	—	—	73.2	100.4	—
J1909−3744	820	Sine	—	0.17(4)	656(33)	9.3	12.4	3.5%
J1909−3744	1500	Both	0.23(5)	0.16(3)	387(11)	6.3	10.2	0.42%
J1918−0642	820	Both	0.19(4)	0.15(2)	601(21)	13.8	17.3	0.7%
B1937+21	820	Sine	—	0.025(5)	368(11)	78.7	109.4	4.4%

refinement using two halves of the band (RM measurements from Yan et al. 2011a detailed in Yan et al. 2011b), whereas we find the RM by using a brute force algorithm that maximizes linear polarization. The techniques give similar uncertainties in the RM but the telescopes used for NANOGrav observations are much larger and more sensitive, which should allow us to determine the RMs with higher precision.

5.1.2. *DM Variations*

Dispersion measure trends are shown in Table 6 and the second panel of Figures 15–23. We detect significant trends in five pulsars (PSRs J1012+5307, J1713+0747, J1744−1134, J1909−3744, and J2302+4442). They all exhibit some kind of linear trend, though four exhibit a sinusoidal trend combined with a linear trend. Our results are similar to those of Jones et al. (2017) for the NANOGrav 9-year data set which used most of the same observational data underlying the present work. There are twelve pulsars that overlap between our data sets, and Jones et al. (2017) finds significant trends in eleven, whereas we only find trends in three. For those pulsars in which we do both find significant trends, the slopes are roughly the same magnitude and the trends are the same for two of them (we find an extra sinusoidal trend in PSR J1012+5307). The differences in our results can be attributed to a lack of overlap in the data sets. Jones et al. (2017) is sensitive to longer term trends because they fit nine years of data, whereas we only include four years in our analysis due to the sampler board issues.

Yan et al. (2011a) also fit DM trends with one year of data from You et al. (2007), though they fit only for linear trends. Their data are not sensitive enough for high-precision DM measurements, and they therefore only report upper limits on the slope of DM variations. For the pulsars that overlap between their paper and this one, they find significant linear trends for three (PSRs J0613−0200, J1024−0719, and B1937+21). We find no significant trends in the DM of any of those pulsars. The fact that we look at data on much longer timescales could cause the discrepancies. Though Yan et al. (2011a) predict that their current slopes are believed to be representative of the longer-term gradients, the linear trends they see are most likely fitted out over longer data sets (which is seen in our analysis).

5.1.3. *Variations in Measured* $\langle B_{\parallel} \rangle$

The magnetic field variations are shown in Table 7 and the third panel of Figures 15–23. We find five pulsars with significant trends (PSRs J0613−0200, J1643−1224, J1713+0747, J1909−3744, J1918−0642, and B1937+21). All show sinusoidal trends, three with a period consistent with a year, and the others with a period of around 600 days. As with the RM variations, we only see two to three full periods in the data set, so these are likely due to stochastic processes and are not true periodicities. As previously noted, because of corrupted data after the sampler board switch, we used a maximum of four years of data for each pulsar.

Four pulsars show significant linear trends in magnetic field. Assuming that this is due to movement through a region of increasing or decreasing B-field, we can use the timescale and amplitude of the trends to calculate the ambient magnetic field over the distance the pulsars have traversed. Local magnetic fields of roughly 10 mG are required over the distances of 82–190 μpc traveled by the pulsar over the timespan of our observations in order to produce the changes in average magnetic field observed.

van Ommen et al. (1997) measured the time variability of the RMs of PSRs B1556−44 and B1727−47 and found that local magnetic fields of 2 μG and 16 μG, respectively, were required to explain the observed variations. The latter was attributed to motion through irregularities within a nearby HII region. Rankin et al. (1988) observed RM and DM variations towards the Crab Pulsar for two years and calculated a local magnetic field of $\sim$170 μG, consistent with its dense magnetic environment. Our values are an order of magnitude larger; it is unlikely these are astrophysical, as our derived fields are much larger than any measured Galactic magnetic fields, even including the 1 mG fields sampled by PSR B1959−63 as it travels through the disk of its companion star (Johnston et al. 2005).

Yan et al. (2011a) point out similarly large derived local B-fields for pulsars for which they measure linear changes in B-field with time (specifically PSRs J0613−0200, J1909−3744, and J2129−5721). However, the method they use to obtain the value of the ambient magnetic field is not correct. Their slopes are also one to two orders of magnitude larger than ours. They point to statistical fluctuations due to random spatial and temporal variations in the interstellar electron density and $\langle B_{\parallel} \rangle$ to explain RM variations. Similarly, the linear trends we derive are likely to be part of larger stochastic trends and not reflective of a linear B-field gradient. Longer and, ideally, more sensitive observations are necessary to discriminate between these possibilities.

You et al. (2012) explored the effects of the Sun on pulsar RM values by observing PSR J1022+1001 when its line-of-sight passed close to the Sun. They found significant effects when the line-of-sight to the pulsar passed below $10\,R_{\odot}$, which corresponds to $\sim$3° of elongation.

We also checked the outliers for large changes in RM, DM, and B-field when the pulsars were at a minimum

elongation. We found that PSR J1614−2230 experiences an increase in all three parameters when it came within 1.3° of the Sun (which corresponds to ∼4.5 $R_\odot$). The increase in RM and DM at minimum elongation corresponds to a solar B-field contribution of 12(1) mG. This is consistent with You et al. (2012) and Ord et al. (2007), who report B-fields of the same order of magnitude at similar distances from the Sun.

5.2. *Microcomponents*

We detect microcomponents in eight of our pulsars. Microcomponents were discussed in Gentile et al. (2018) and here we define them as components that are not easily visible in the average profile and/or are <4% of the intensity of the highest peak on the average profile. Out of these eight, three pulsars have microcomponents that are detected for the first time. Most of the microcomponents, such as that of PSRs B1937+21 (820 MHz) and J2145−0740 (820 MHz), have a high degree of polarization, but others, such as that of PSR J1909−3744, exhibit very little.

Microcomponents that have been previously detected in other works have a flux density of above 1.6 mJy, and all of the new ones have a flux density of ≤ 1.5 mJy and below. Because of our long data sets, which produce a very high S/N composite profiles, we are able to detect these very faint microcomponents. When the set of observations is temporally split into two, the microcomponents are detected in both halves. We also see the microcomponents in the upper and lower half of each frequency band and with the exception of J1713+0747 (see Section 4.15), they are seen at both 820 MHz and 1500 MHz for each pulsar. The tests show that microcomponents are not an anomalous instrumental artifact but are rather most likely of astrophysical origin. The detection of microcomponents demonstrates that MSPs emit over a wide phase range due to their larger opening angles and emission produced further out in the magnetosphere (Xilouris et al. 1998).

These microcomponents make it difficult to define the duty cycle of millisecond pulsars. As noted in Gentile et al. (2018), they may cause an overestimation of the radiometer noise in the off-pulse region which would affect flux calibration (something NANOGrav does not rely on). If these microcomponents are present in other pulsars, they would be revealed by longer data sets (and therefore higher S/N profiles). Microcomponents are generally most prevalent in our highest S/N pulsars; higher gain telescopes would improve that S/N, allowing us to probe weaker pulsars for these microcomponents (e.g., Spiewak et al. in prep.). To make template profiles for TOAs, NANOGrav aligns and averaged the reduced data profiles and applies wavelet smoothing to the average profile (Alam et al. 2020). This wavelet smoothing preserves the microcomponents, and therefore they are taken into account when calculating TOAs.

5.3. *Emission Geometry*

As expected, the polarization profiles for these millisecond pulsars are very complex, as is the position angle sweep (which is shown in the top panel of Figures 3–14 above the profiles). The position angle in PSRCHIVE is plotted when the linear polarization is $>3\sigma$.

Many pulsars show very complex polarization angle sweeps (e.g. PSRs J1455−3330, J1918−0642, and J2145−0750) that would require a model more sophisticated than the RVM. Only two pulsars in our data set show a quasi-S-shaped curve in the PA. Using PSRCHIVE, we searched an 18 by 18 grid in which α (the angle between the spin axis and the magnetic axis) and ζ (the sum of α and the angle between the magnetic axis and sightline β) are varied from 5 to 175 degrees in steps of 10 degrees. We perform this fitting for both pulsars at each frequency. The only significant result is the L-band observation of PSR J1600−3053, where $\alpha = 52.8 \pm 5.0$, $\beta = 49.6 \pm 14.6$, a fit that has a χ^2_r value of 2.5. This shows that PAs are very difficult to fit in MSPs and a more sophisticated model incorporating emission far from the polar caps and/or more complex magnetic field structures is required to fit the position angle sweeps. Craig & Romani (2012) and Craig (2014b) show that by adding in the sweep of the phase shift, fitting an RVM may be possible.

5.4. *Correlations with Pulsar Parameters*

Studies such as Johnston & Kerr (2018) have examined the correlation between polarization fraction and spin-down parameters, but none have been conclusive. Using the wealth of polarization information in this study, we examine the relationship between linear and circular polarization and five parameters: spin period, age, surface dipole magnetic field, spin down energy loss, and proper motion. We find no conclusive evidence of any correlations between these parameters and linear or circular polarization fraction 820 MHz or 1500 MHz. If a relation did arise, it would give information about the magnetosphere, pointing to the fact that MSPs, for instance, with different spin periods have different sized magnetospheres.

5.5. *Timing Implications*

Pulsar time-of-arrival measurements calculated from data which have not been corrected for telescope polarization distortions, such has the NANOGrav 12.5-year

data set (Alam et al. 2020), are susceptible to systematic timing errors. These errors will be higher for pulsars with larger polarization fractions (see Table 3). Correction of these data using the Mueller matrix formulation, as in the present paper, has the potential to improve the timing accuracy of such data sets. Also note that while incorrect polarization calibration could lead to higher levels of noise in the dataset, it would not show the spatial correlations expected for a GW signature. Future work will apply the methods outlines in this paper to NANOGrav data our to determine the effect of polarization-calibrated profiles on timing.

These data only represent a portion of those obtained by the NANOGrav timing campaign. New ultra-wideband receivers on the GBT will provide more sensitivity. The Canadian HI Mapping Experiment (CHIME) telescope will provide complementary frequency coverage to track how the polarization and microcomponents behave at lower frequencies.

6. ACKNOWLEDGEMENTS

We thank the double pulsar team (M. Kramer, N. Pol, R. Ferdman, A. Possenti, P. Freire) for sharing their B1929+10 data with us. We also thank Dr. James McKee for useful conversations regarding this work. This research was made possible by NASA West Virginia Space Grant Consortium, NASA Agreement #80NSSC20M0055. This work was also supported by NSF Award OIA-1458952. The Green Bank Observatory is a facility of the NSF operated under cooperative agreement by Associated Universities, Inc. The NANOGrav project receives support from National Science Foundation (NSF) Physics Frontiers Center award number 1430284. Work on NANOGrav at NRL is supported by ONR 6.1 basic research funding. TD and ML acknowledge NSF AAG award number 2009468. KC is supported by a UBC Four Year Fellowship (6456).

Author Contributions: HMW carried out the analysis and prepared the text, figures, and tables. MAM helped with the development of the framework and the text. PAG helped with the development of the framework. MLJ helped with the analyses and code. RS assisted with the analysis and the discussion. All authors contributed to the collection and analysis of the NANOGrav 12.5-year data set; see Alam et al. (2020) for further details.

Software: numpy (Oliphant 2006; Van Der Walt et al. 2011), matplotlib (Hunter 2007), PSRCHIVE (Hotan et al. 2004)

REFERENCES

Alam, M. F., et al. 2020, arXiv e-prints, arXiv:2005.06490. https://arxiv.org/abs/2005.06490

Arzoumanian, Z., et al. 2018, ApJS, 235, 37, doi: 10.3847/1538-4365/aab5b0

Bangale, P. 2011, Master's thesis, Chalmers University of Technology

Brook, P. R., Karastergiou, A., McLaughlin, M. A., et al. 2018, ApJ, 868, 122, doi: 10.3847/1538-4357/aae9e3

Burgay, M., Bailes, M., Bates, S., et al. 2013, Monthly Notices of the Royal Astronomical Society, 433, 259, doi: 10.1093/mnras/stt721

Craig, H. A. 2014a, ApJ, 790, 102, doi: 10.1088/0004-637X/790/2/102

—. 2014b, ApJ, 790, 102, doi: 10.1088/0004-637X/790/2/102

Craig, H. A., & Romani, R. W. 2012, ApJ, 755, 137, doi: 10.1088/0004-637X/755/2/137

Dai, S., Hobbs, G., Manchester, R. N., et al. 2015, MNRAS, 449, 3223, doi: 10.1093/mnras/stv508

Dike, V., Taylor, G. B., Dowell, J., & Stovall, K. 2020, arXiv e-prints, arXiv:2006.10140. https://arxiv.org/abs/2006.10140

Dolch, T., Lam, M. T., et al. 2014, ApJ, 794, 21, doi: 10.1088/0004-637X/794/1/21

Gentile, P. A., McLaughlin, M. A., Demorest, P. B., et al. 2018, ApJ, 862, 47, doi: 10.3847/1538-4357/aac9c9

Guillot, S., Kerr, M., et al. 2019, ApJL, 887, L27, doi: 10.3847/2041-8213/ab511b

Heiles, C., Perillat, P., Nolan, M., et al. 2001, PASP, 113, 1274, doi: 10.1086/323289

Hotan, A. W., Bailes, M., & Ord, S. M. 2004, MNRAS, 355, 941, doi: 10.1111/j.1365-2966.2004.08376.x

Hotan, A. W., van Straten, W., & Manchester, R. N. 2004, Publications of the Astronomical Society of Australia, 21, 302–309, doi: 10.1071/AS04022

Hunter, J. D. 2007, Computing in Science Engineering, 9, 90

Johnston, S., Ball, L., Wang, N., & Manchester, R. N. 2005, MNRAS, 358, 1069, doi: 10.1111/j.1365-2966.2005.08854.x

Johnston, S., & Kerr, M. 2018, MNRAS, 474, 4629, doi: 10.1093/mnras/stx3095

Jones, M. L., McLaughlin, M. A., et al. 2017, ApJ, 841, 125, doi: 10.3847/1538-4357/aa73df

Kramer, M., Xilouris, K. M., et al. 1998, ApJ, 501, 270, doi: 10.1086/305790

Manchester, R. N., & Han, J. L. 2004, ApJ, 609, 354, doi: 10.1086/420918

NANOGrav Collaboration, et al. 2015, ApJ, 813, 65, doi: 10.1088/0004-637X/813/1/65

Noutsos, A., Sobey, C., Kondratiev, V., et al. 2015, A&A, 576, A62, doi: 10.1051/0004-6361/201425186

Oliphant, T. E. 2006, A guide to NumPy, Vol. 1 (Trelgol Publishing USA)

Ord, S. M., Johnston, S., & Sarkissian, J. 2007, SoPh, 245, 109, doi: 10.1007/s11207-007-9030-6

Ord, S. M., van Straten, W., Hotan, A. W., & Bailes, M. 2004, MNRAS, 352, 804, doi: 10.1111/j.1365-2966.2004.07963.x

Radhakrishnan, V., & Cooke, D. J. 1969, Astrophys. Lett., 3, 225

Rankin, J. M. 1993, ApJ, 405, 285, doi: 10.1086/172361

Rankin, J. M., Campbell, D. B., Isaacman, R. B., & Payne, R. R. 1988, A&A, 202, 166

Rickett, B. J. 1990, ARA&A, 28, 561, doi: 10.1146/annurev.aa.28.090190.003021

Scargle, J. D. 1982, ApJ, 263, 835, doi: 10.1086/160554

Sobey, C., Bilous, A. V., Grießmeier, & others. 2019, MNRAS, 484, 3646, doi: 10.1093/mnras/stz214

Sotomayor-Beltran, C., Sobey, C., Hessels, J., et al. 2013, A&A, 552, A58, doi: 10.1051/0004-6361/201220728

Stairs, I. H., Thorsett, S. E., & Camilo, F. 1999, ApJS, 123, 627, doi: 10.1086/313245

Stokes, G. G. 1851, Transactions of the Cambridge Philosophical Society, 9, 399

Van Der Walt, S., Colbert, S. C., & Varoquaux, G. 2011, Computing in Science & Engineering, 13, 22

van Ommen, T. D., D'Alessandro, F., Hamilton, P. A., & McCulloch, P. M. 1997, MNRAS, 287, 307, doi: 10.1093/mnras/287.2.307

van Straten, W. 2004, ApJS, 152, 129, doi: 10.1086/383187

van Straten, W., Demorest, P., & Oslowski, S. 2012, Astronomical Research and Technology, 9, 237. https://arxiv.org/abs/1205.6276

Xilouris, K. M., Kramer, M., et al. 1998, ApJ, 501, 286, doi: 10.1086/305791

Yan, W. M., Manchester, R. N., Hobbs, G., van Straten, W., et al. 2011a, Ap&SS, 335, 485, doi: 10.1007/s10509-011-0756-0

Yan, W. M., Manchester, R. N., van Straten, W., Reynolds, J. E., et al. 2011b, MNRAS, 414, 2087, doi: 10.1111/j.1365-2966.2011.18522.x

You, X. P., Coles, W. A., Hobbs, G. B., & Manchester, R. N. 2012, MNRAS, 422, 1160, doi: 10.1111/j.1365-2966.2012.20688.x

You, X. P., Hobbs, G., Coles, W. A., et al. 2007, MNRAS, 378, 493, doi: 10.1111/j.1365-2966.2007.11617.x

Figure 3. Pulse profile for pulsars J0340+4130 and J0613–0200. The black line is the total intensity, red is the circular polarization, and blue is the circular polarization. The polarization position angle is shown in the top panel.

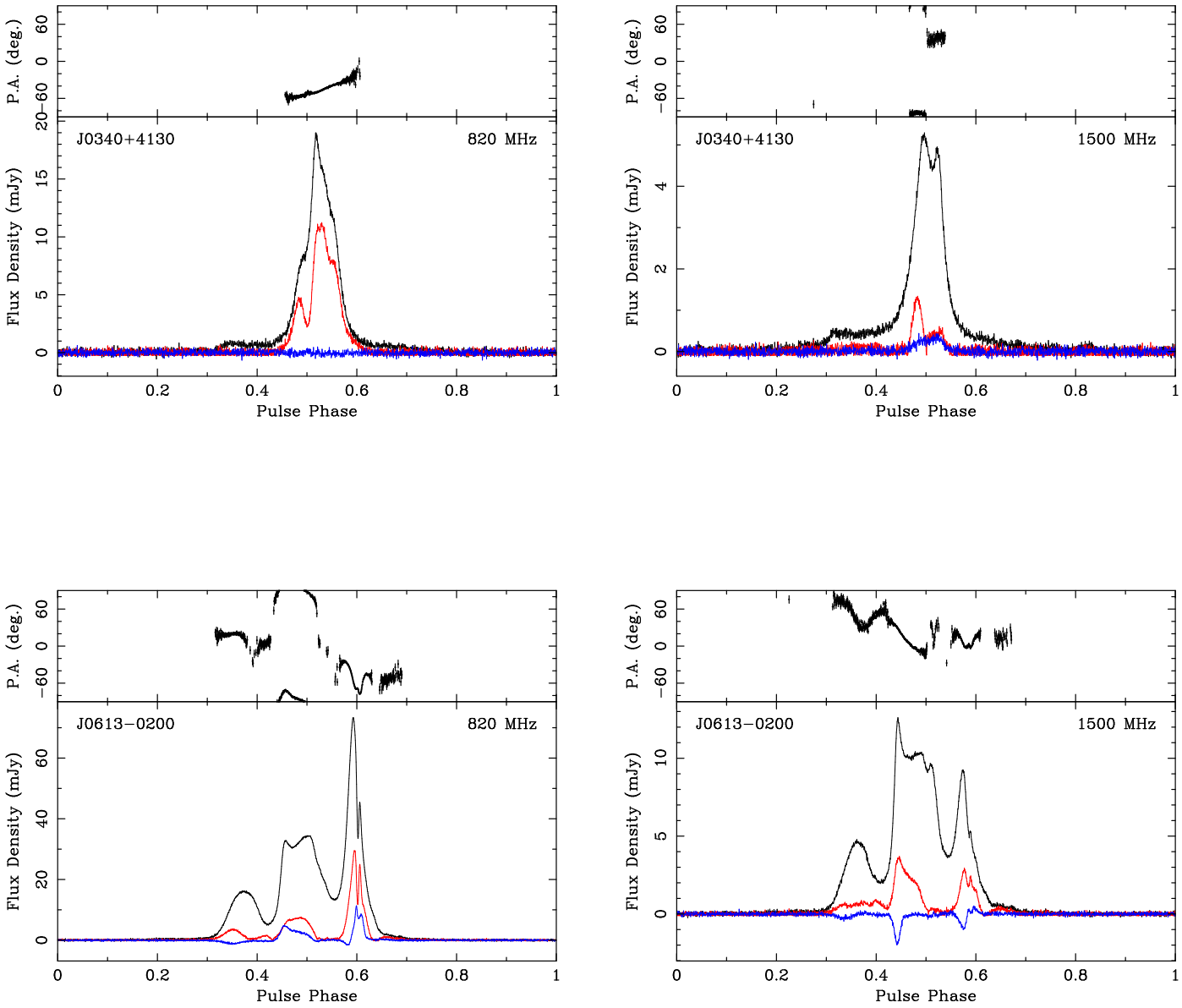

Figure 4. The pulse profile for pulsars J0636+5128 and J0645+5158. The black line is the total intensity, red is the linear polarization, and blue is the circular polarization. The polarization position angle is shown in the top panel.

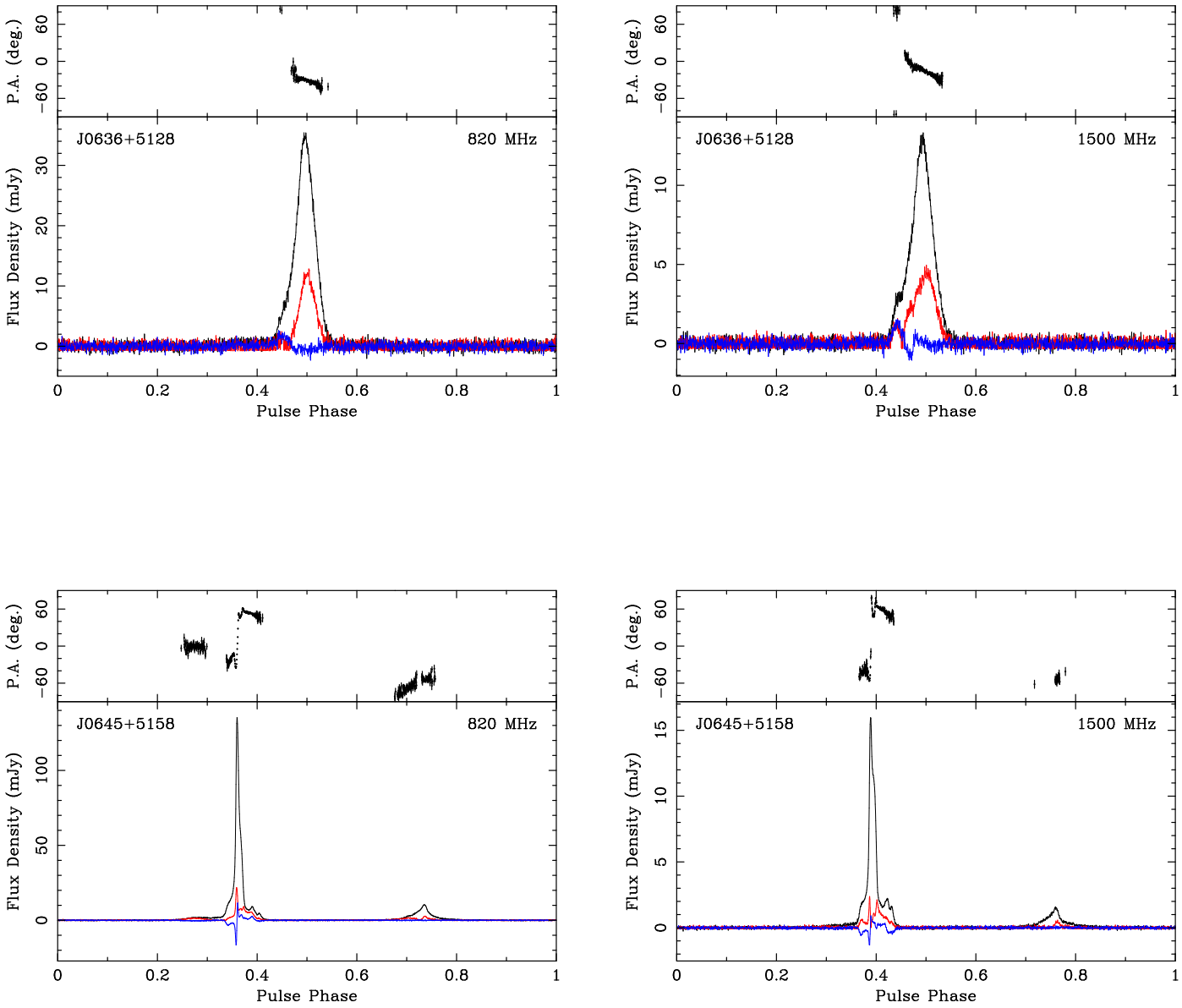

Figure 5. Pulse profiles for pulsars J0740+6620 and J0931–1902. The black line is the total intensity, red is the linear polarization, and blue is the circular polarization. The polarization position angle is shown in the top panel.

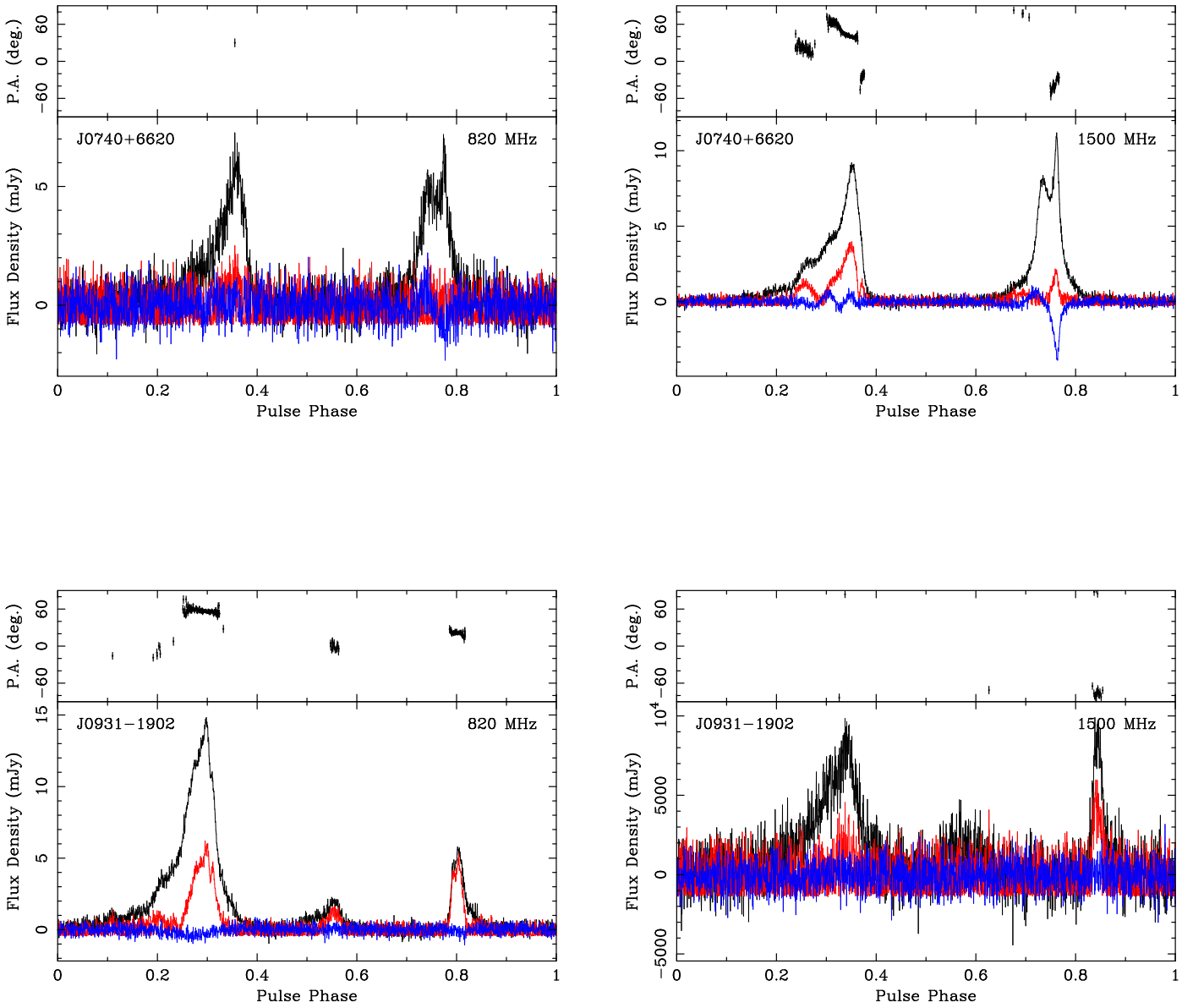

Figure 6. Pulse profiles for pulsars J1012+5307 and J1024–0719 including microcomponents. The black line is the total intensity, red is the linear polarization, and blue is the circular polarization. The black arrow points to the location of the microcomponent in J1024–0719. The polarization position angle is shown in the top panel. The microcomponent plots for J1024–0719 have been plotted with fewer bins to increase the signal-to-noise. The polarization position angle is shown in the top panel.

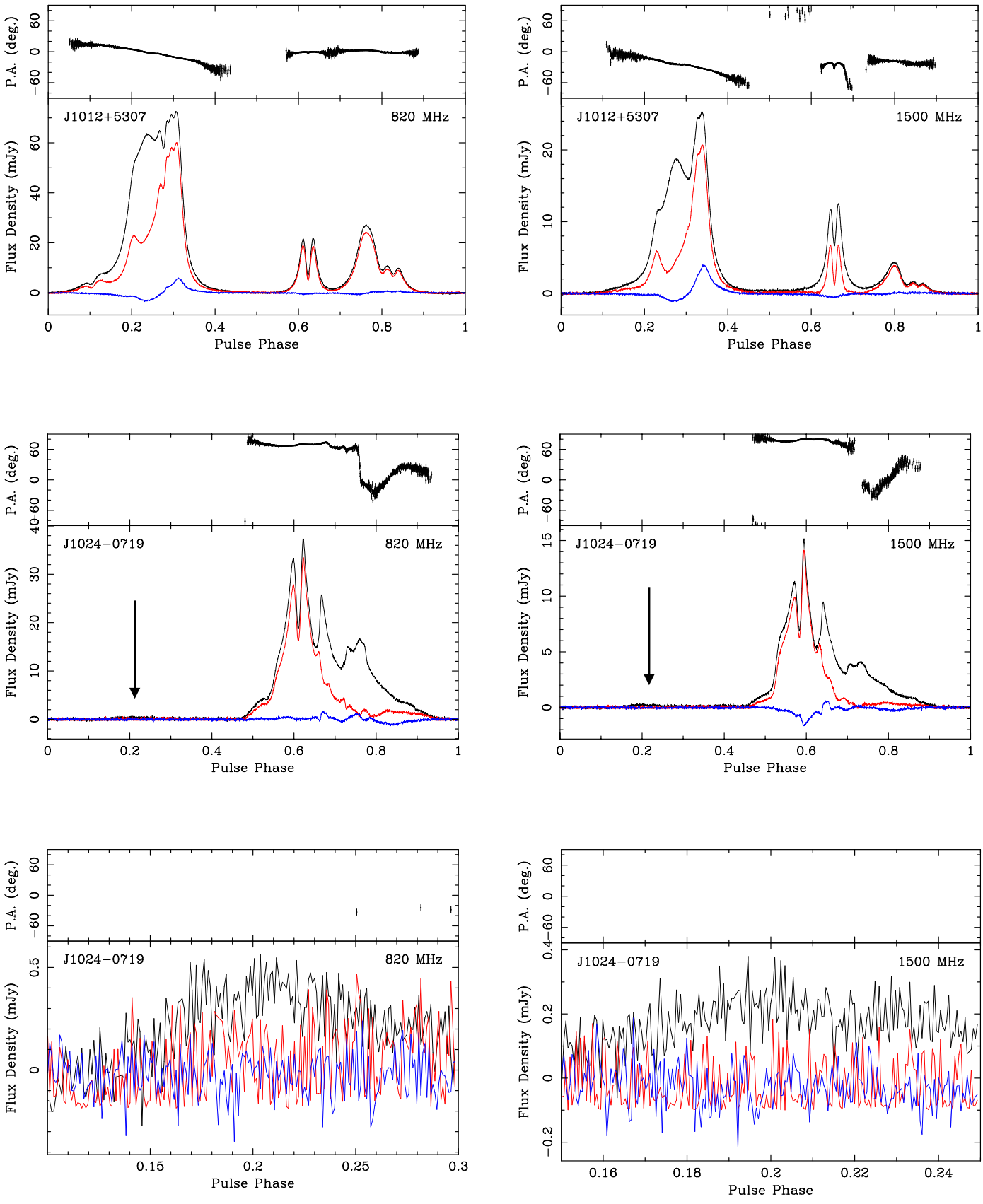

Figure 7. Pulse profiles for pulsars J1125+7819 and J1455–3330 including microcomponents. The black line is the total intensity, red is the linear polarization, and blue is the circular polarization. The black arrow points to the location of the microcomponent of J1455–3330. The microcomponent plots for J1455–3330 have been plotted with fewer bins increase the signal-to-noise. The polarization position angle is shown in the top panel.

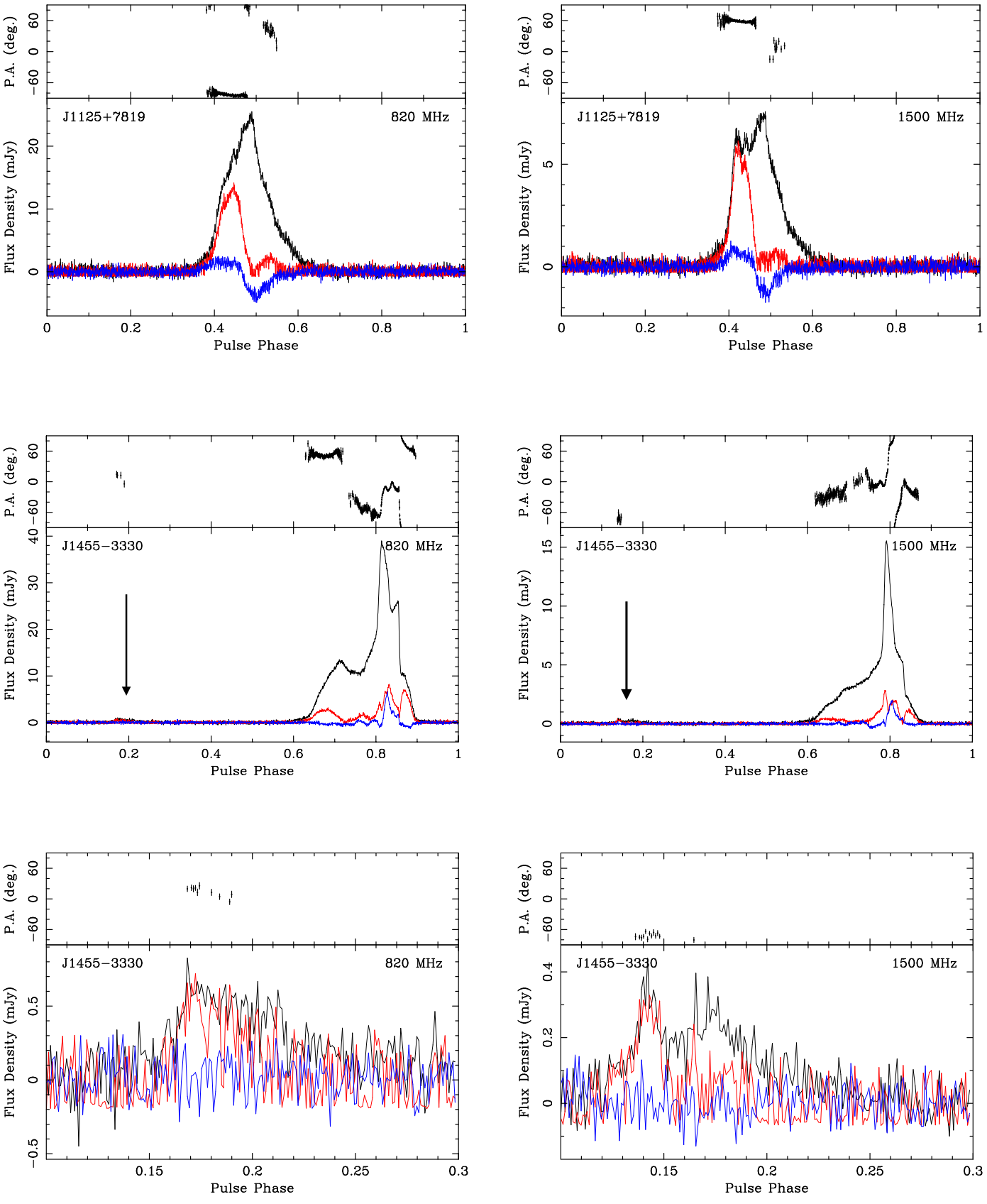

Figure 8. Pulse profiles for pulsars J1600–3053 and J1614–3053 including microcomponents. The black line is the total intensity, red is the linear polarization, and blue is the circular polarization. The black arrow points to the location of the microcomponent of J1600–3053. The microcomponent plots for J1455–3330 have been plotted with fewer bins increase the signal-to-noise. The polarization position angle is shown in the top panel.

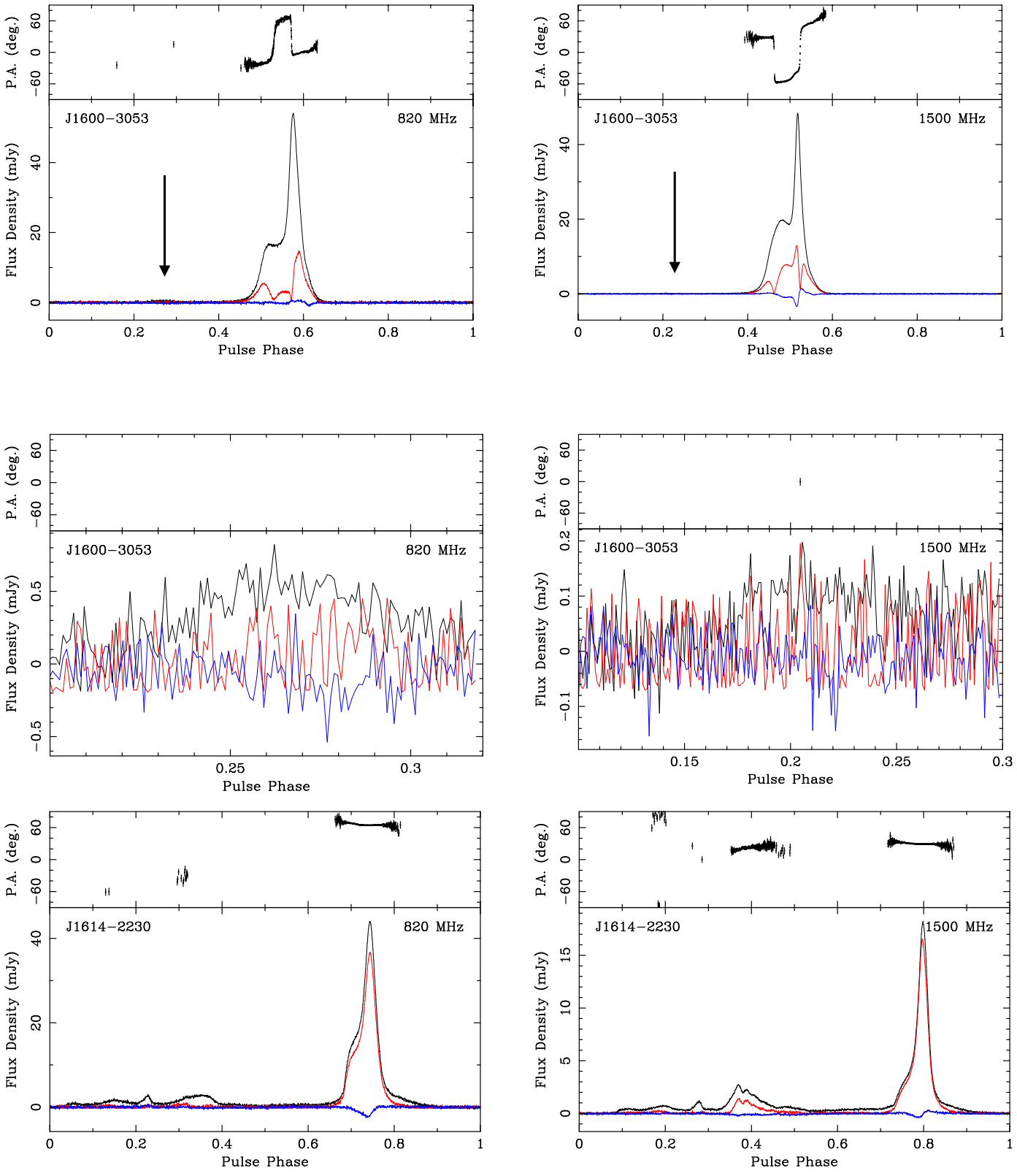

Figure 9. Pulse profiles for pulsars J1643–1224 and J1713+0747 including microcomponents. The black line is the total intensity, red is the linear polarization, and blue is the circular polarization. The black arrow points to the location of the microcomponent in each J1713+0747 profile. The microcomponent plot for J1713–0747 have been plotted with fewer bins to increase the signal-to-noise. The polarization position angle is shown in the top panel. Note: there is no detection of the microcomponent of J1713+0747 at 820 MHz, the plot is just shown for comparison.

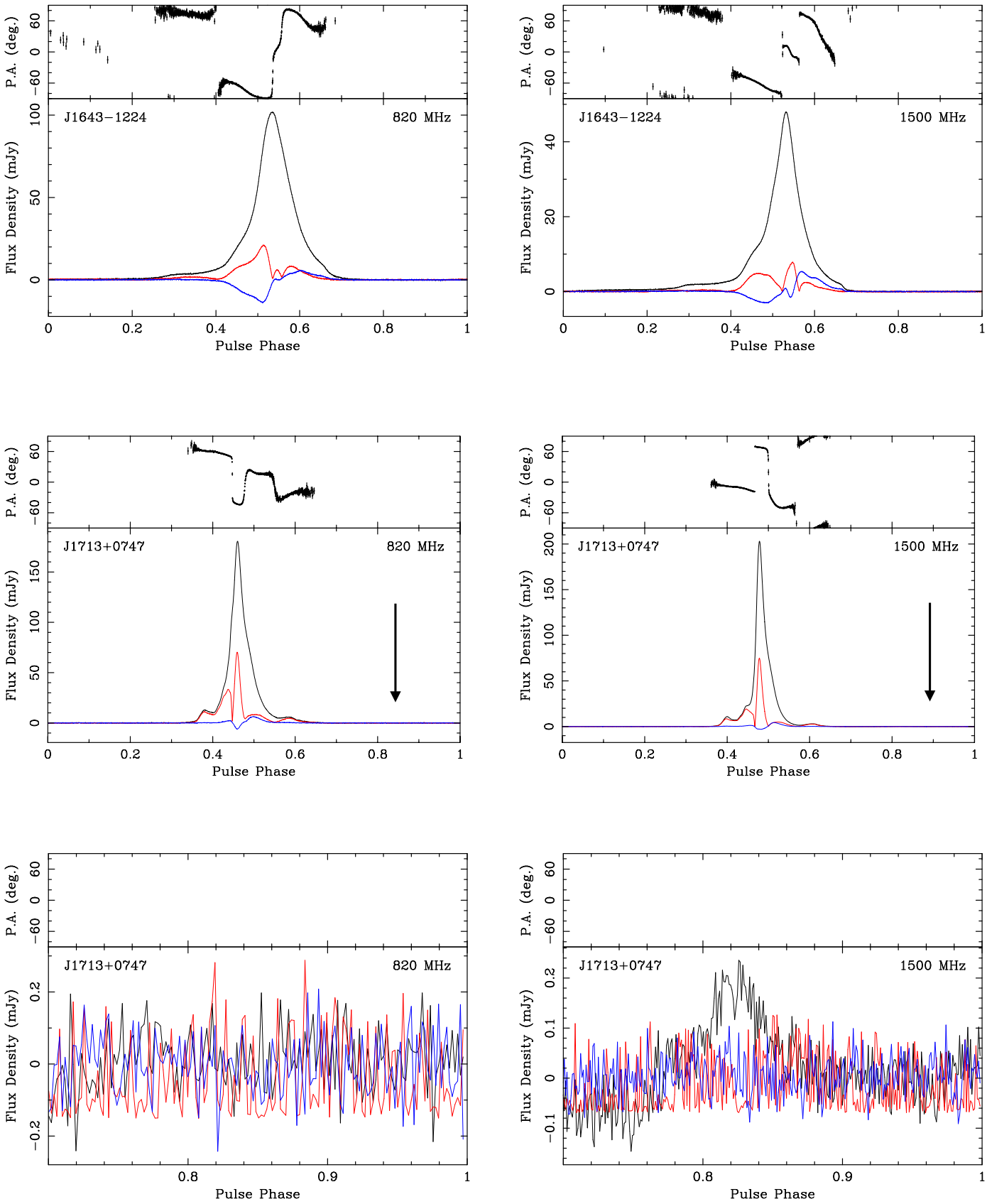

Figure 10. Pulse profiles for pulsars J1744–1134 and J1747–4036. The black line is the total intensity, red is the linear polarization, and blue is the circular polarization. The polarization position angle is shown in the top panel.

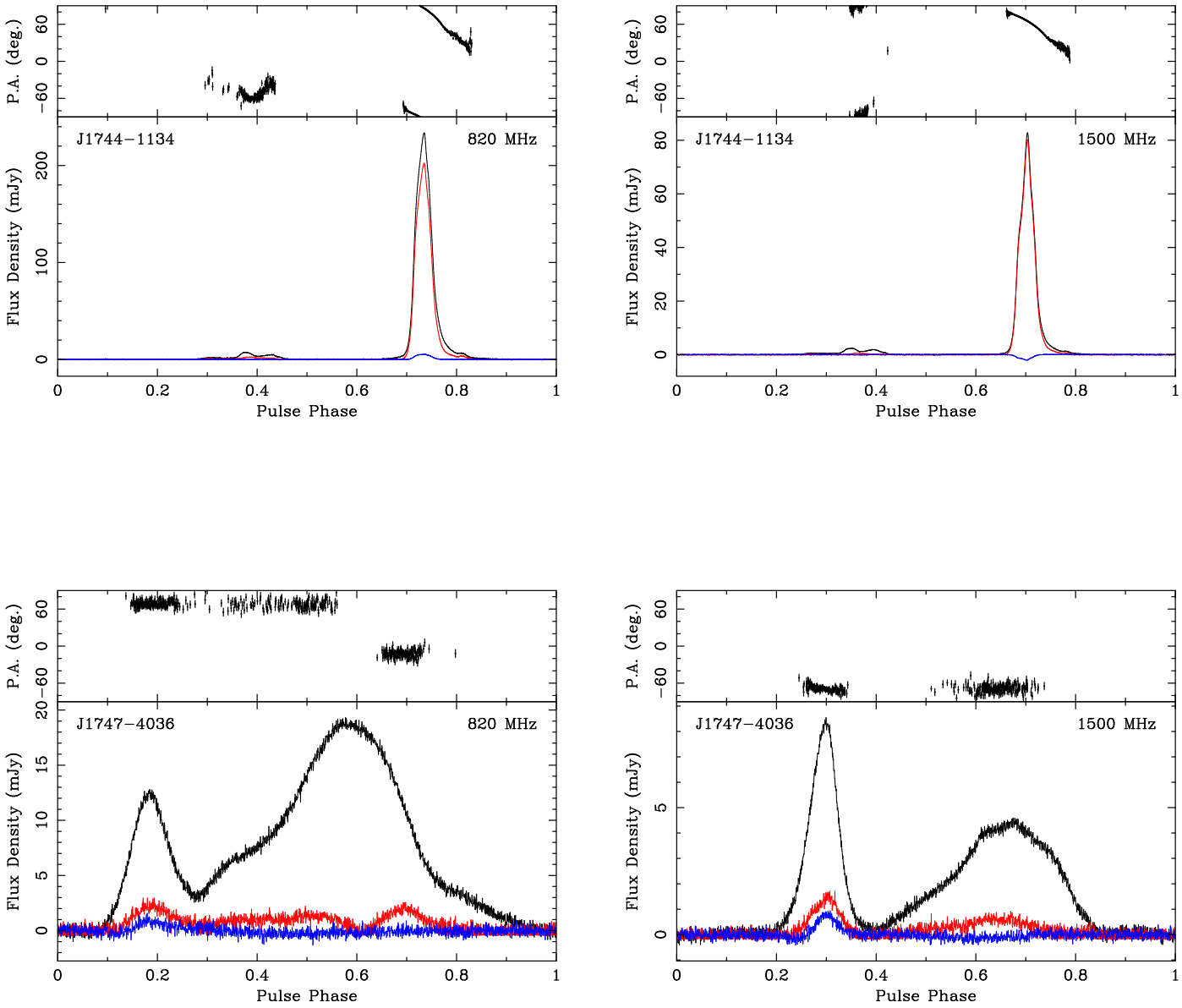

Figure 11. Pulse profiles for pulsars J1832–0836 and J1909–3744 including microcomponents. The black line is the total intensity, red is the linear polarization, and blue is the circular polarization. The black arrow points to the location of the microcomponent in each J1909–3744 profile. The polarization position angle is shown in the top panel.

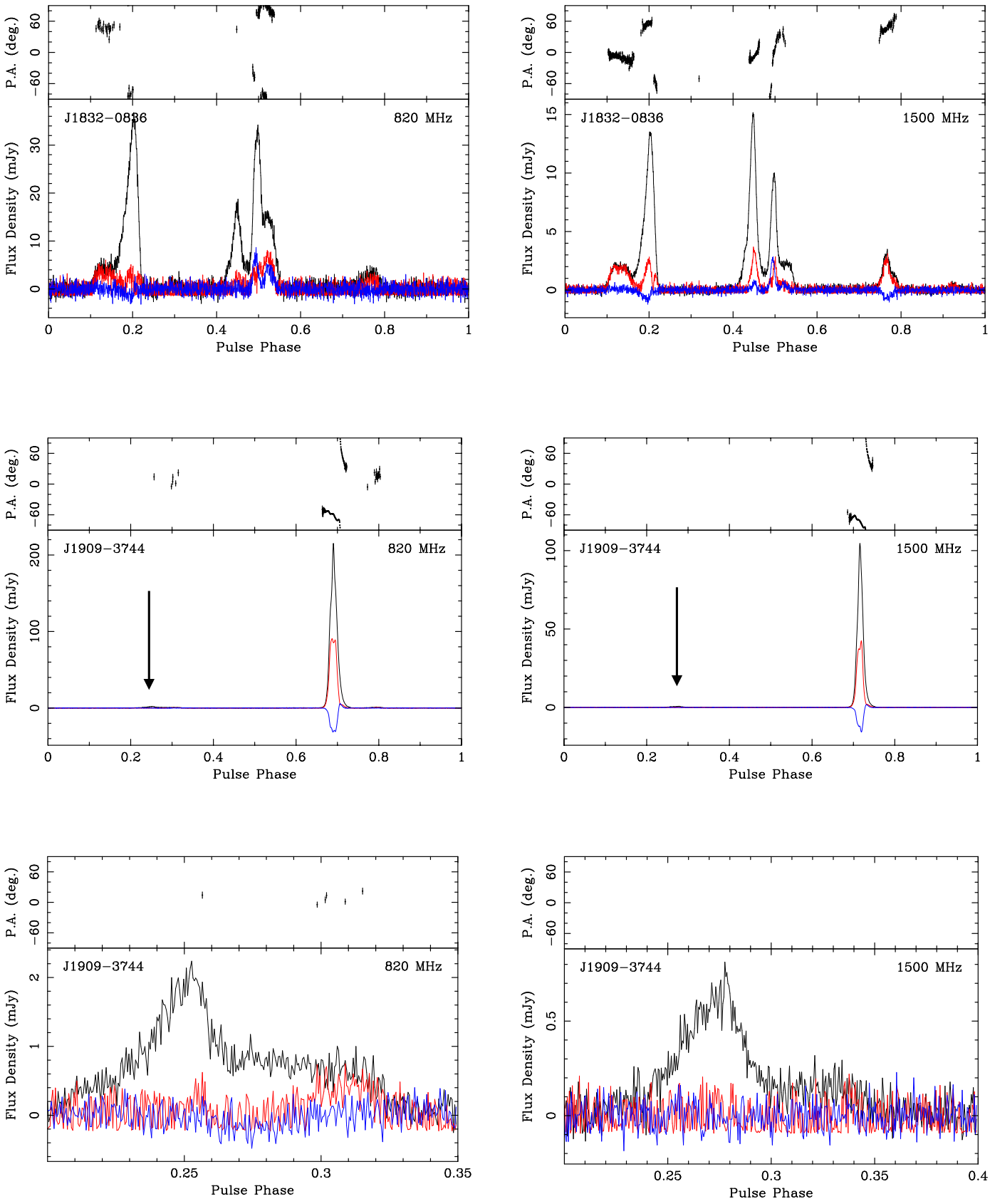

Figure 12. Pulse profile for pulsars J1918–0642 and B1937+21 including microcomponents. The black arrow points to the location of the microcomponent in each B1937+21 profile. The black line is the total intensity, red is the linear polarization, and blue is the circular polarization. The polarization position angle is shown in the top panel.

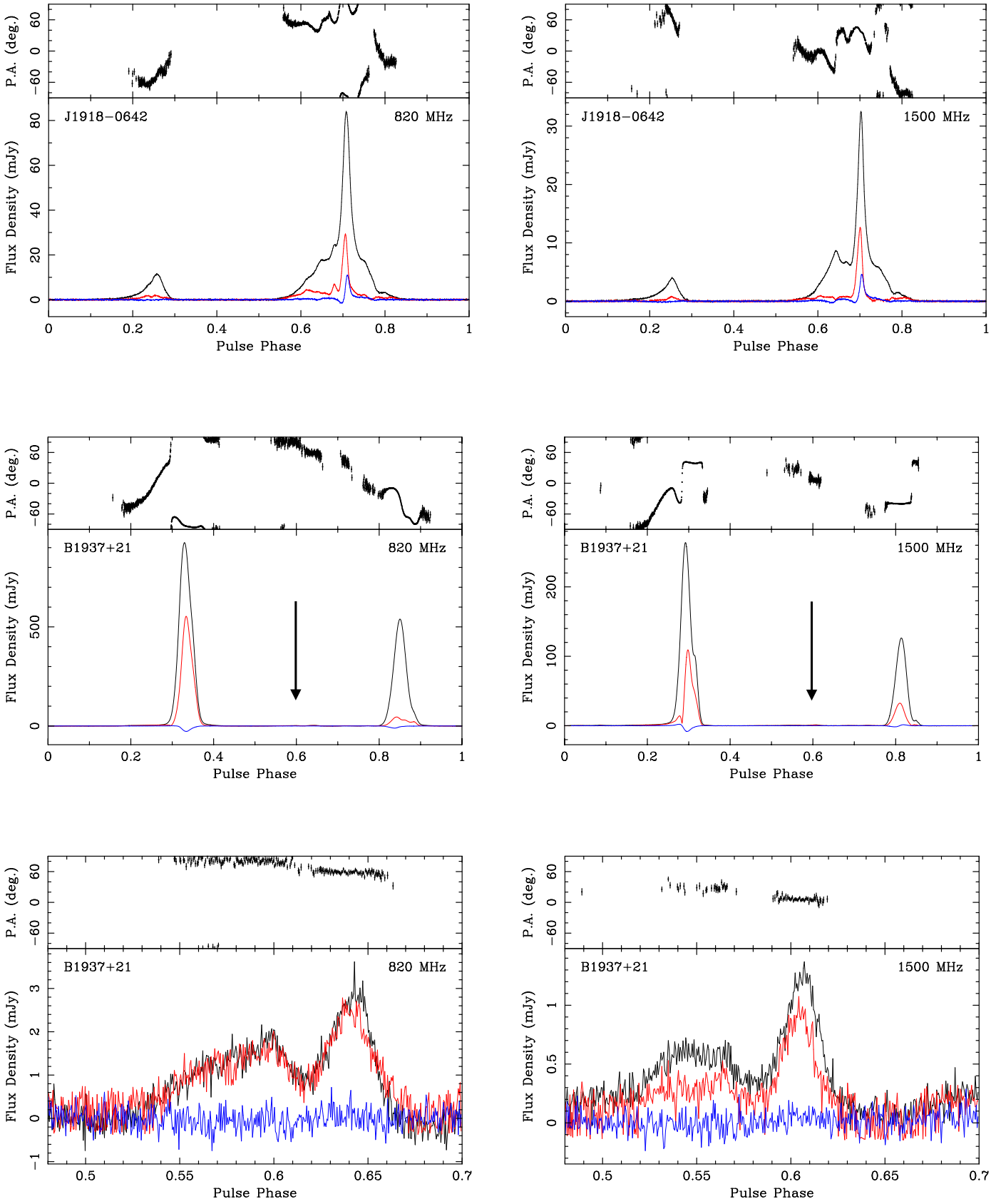

Figure 13. Pulse profiles for pulsars J2010–1323 and J2145–0750 including microcomponents. The black arrow points to the location of the microcomponent in each J2145–0750 profile. The black line is the total intensity, red is the linear polarization, and blue is the circular polarization. The polarization position angle is shown in the top panel.

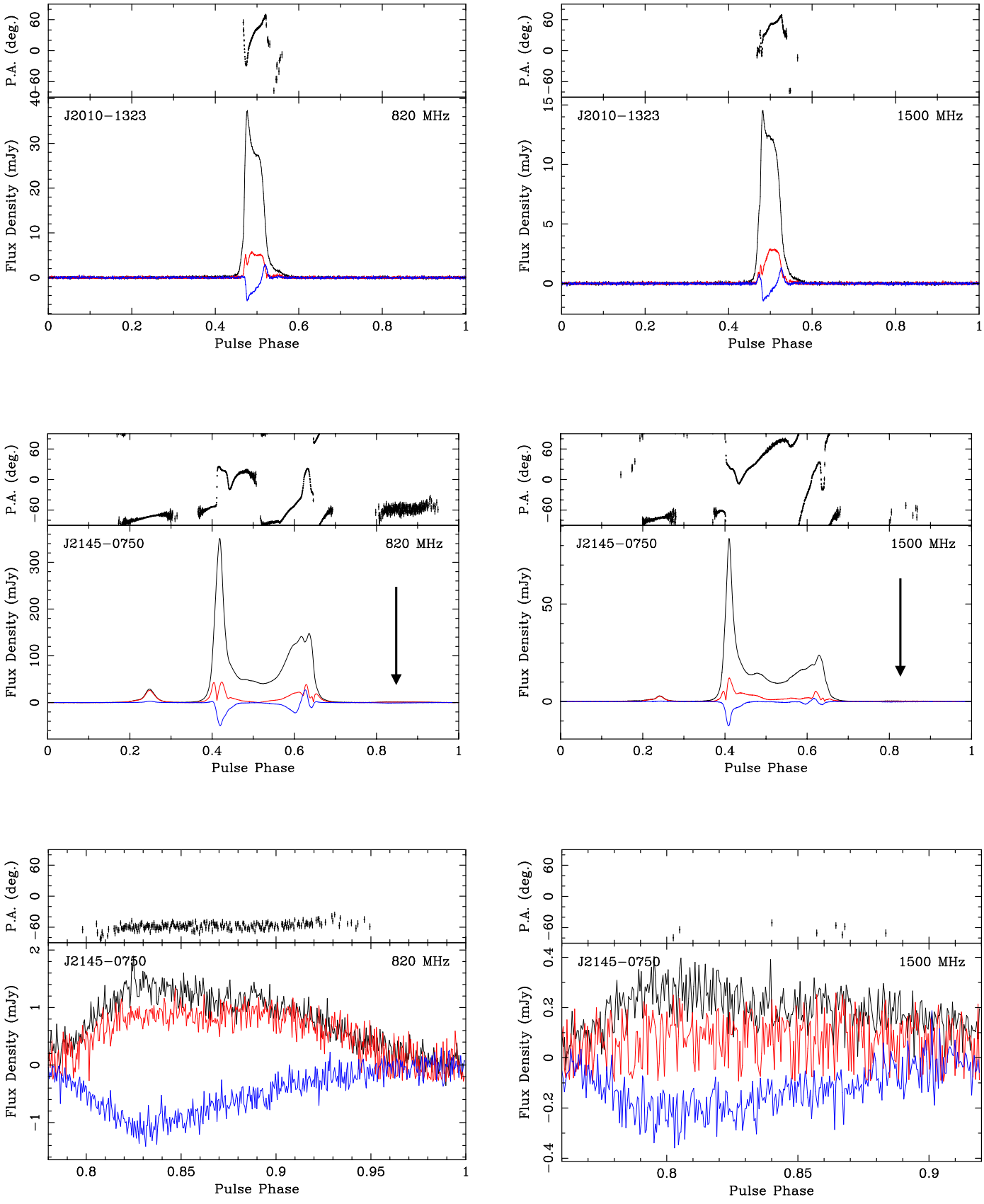

Figure 14. Pulse profiles for pulsars J2302+4442. The black line is the total intensity, red is the linear polarization, and blue is the circular polarization. The polarization position angle is shown in the top panel.

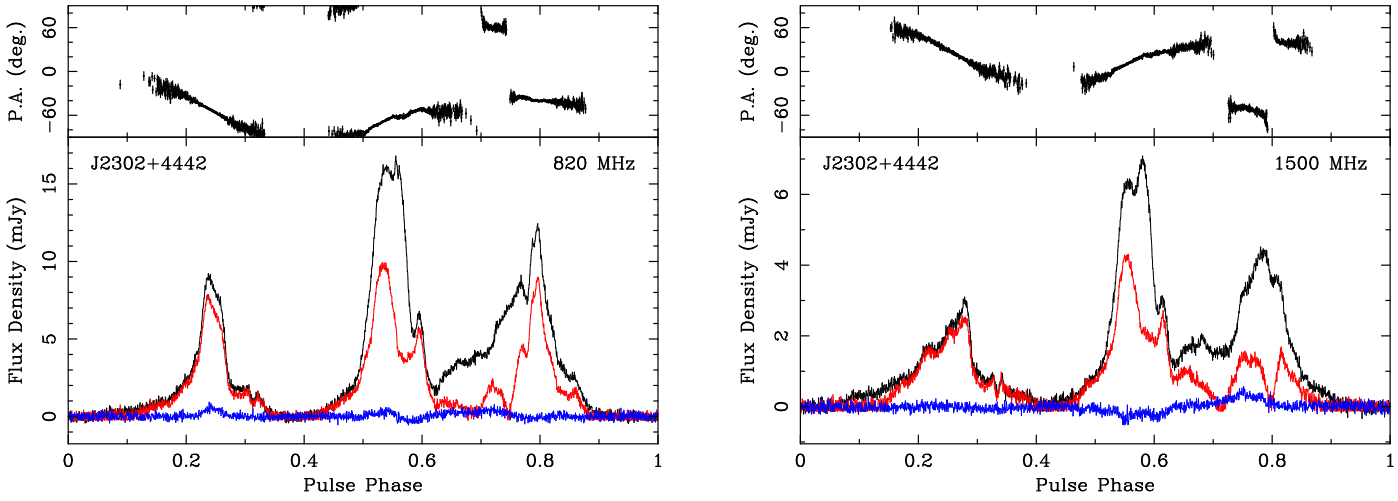

Figure 15. Ionosphere-corrected rotation measure, dispersion measure, and magnetic field changes over time for pulsars J0340+4130 and J0613–0200. The error bars on the RM are a combination of fitting for Faraday rotation and from the ionospheric correction, errors on the DM come from those on the DMX value are those reported by TEMPO, and errors on the magnetic field are a combination of the two. The trendline shown is that with the lowest reduced χ^2_r value of all of the trends. No trend is shown if the lowest χ^2_r value for the fits was that of a horizontal line with a slope of zero.

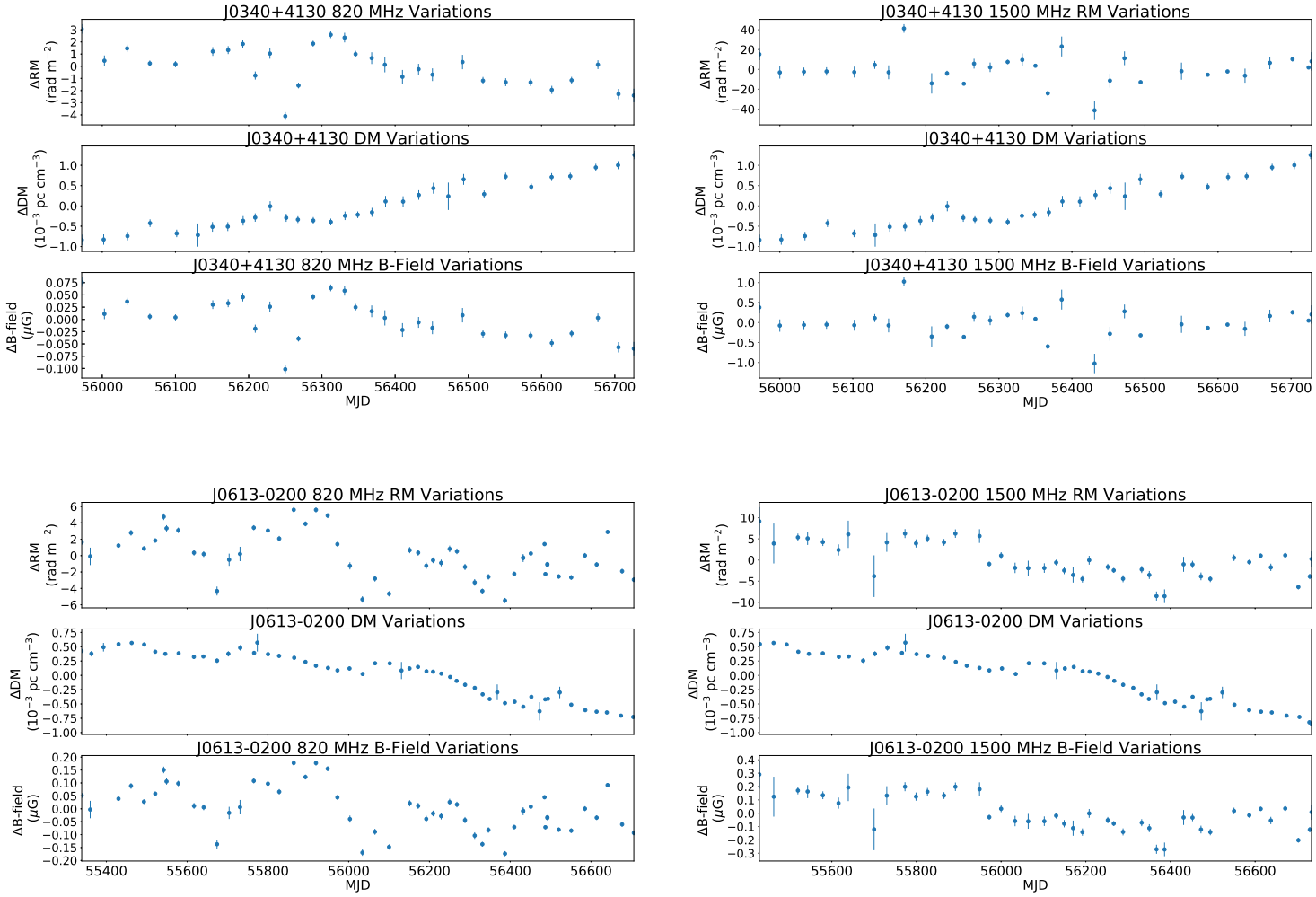

Figure 16. Ionosphere-corrected rotation measure, dispersion measure, and magnetic field variations over time for pulsars J0645+5158 and J1012+5307. The error bars on the RM are a combination of fitting for Faraday rotation and from the ionospheric correction, errors on the DM come from those on the DMX value, and errors on the magnetic field are a combination of the two. The trendline shown is that with the lowest reduced χ^2_r value of all of the trends. No trend is shown if the lowest χ^2_r value for the fits was that of a horizontal line with a slope of zero.

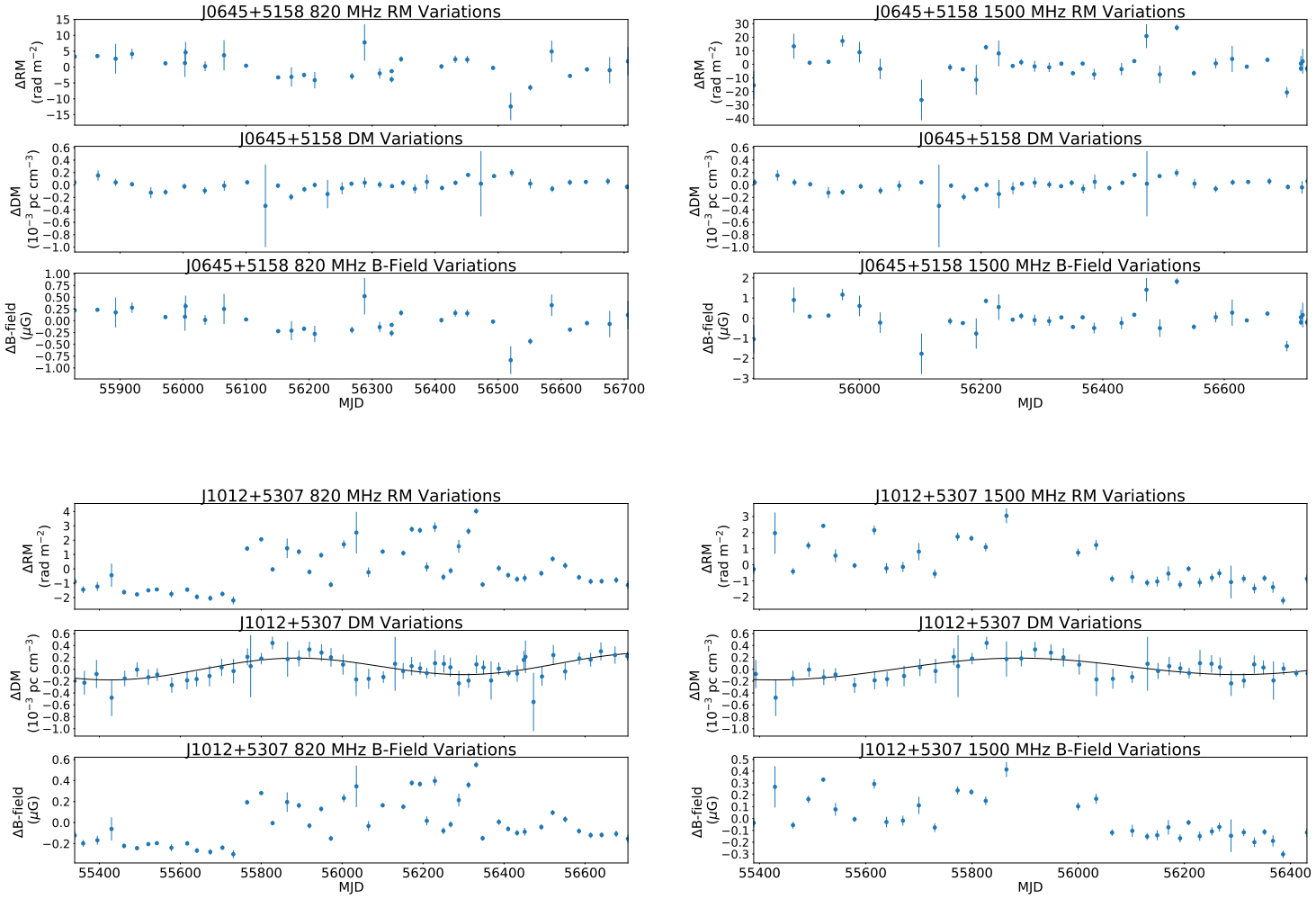

Figure 17. Ionosphere-corrected rotation measure, dispersion measure, and magnetic field changes over time for pulsars J1024–0719 and J1455–3330. The error bars on the RM are a combination of fitting for Faraday rotation and from the ionospheric correction, errors on the DM come from those on the DMX value, and errors on the magnetic field are a combination of the two. The trendline shown is that with the lowest reduced χ^2_r value of all of the trends. No trend is shown if the lowest χ^2_r value for the fits was that of a horizontal line with a slope of zero.

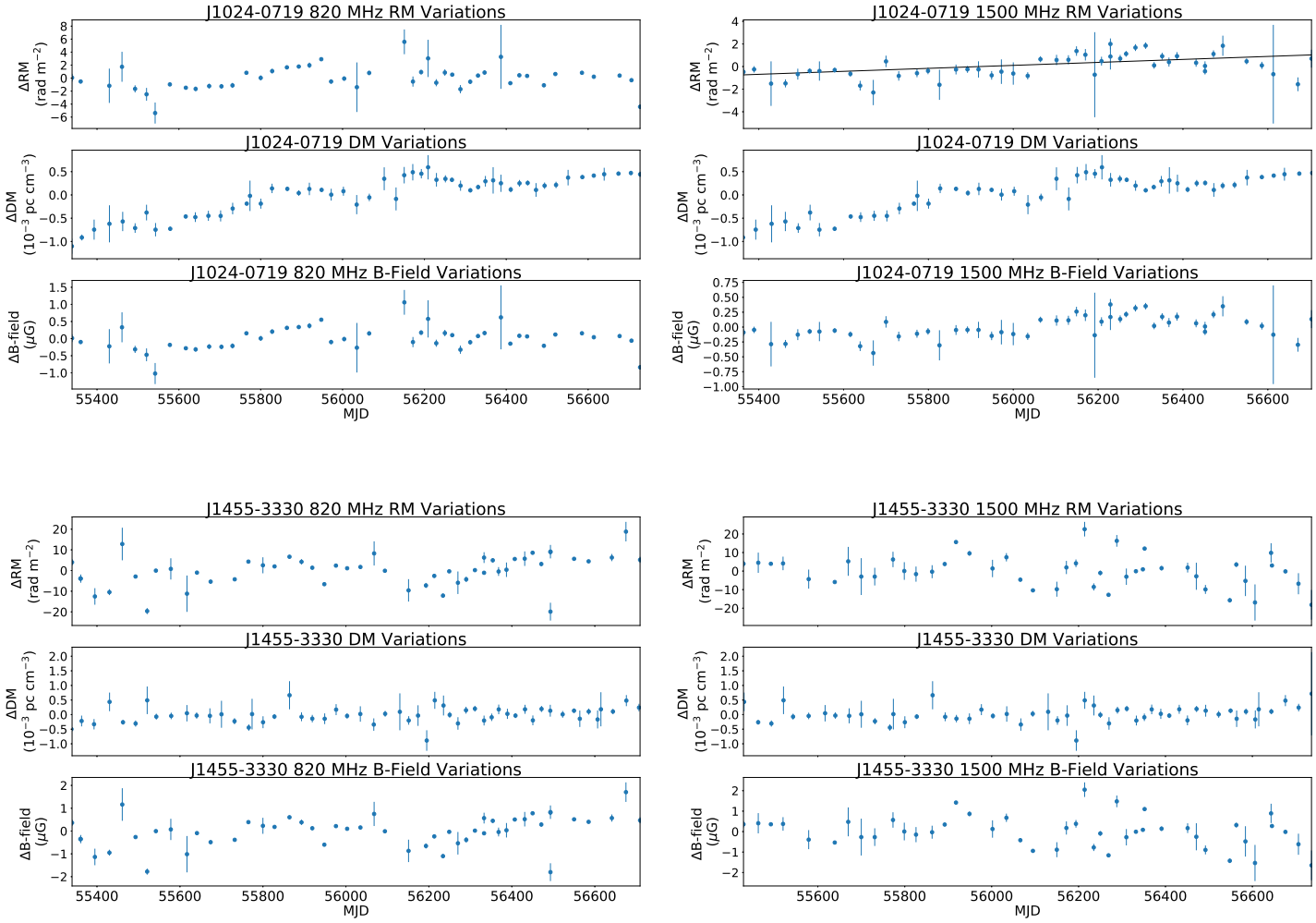

Figure 18. Ionosphere-corrected rotation measure, dispersion measure, and magnetic field changes over time for pulsars J1600–3053 and J1614–2230. The error bars on the RM are a combination of fitting for Faraday rotation and from the ionospheric correction, errors on the DM come from those on the DMX value, and errors on the magnetic field are a combination of the two. The trendline shown is that with the lowest reduced χ^2_r value of all of the trends. No trend is shown if the lowest χ^2_r value for the fits was that of a horizontal line with a slope of zero. Note: the plots for J1614–2203 contain two outliers at epochs of small ecliptic angle (less than 3 degrees) (MJDs 55892 and 55893, as discussed in Section 5.1.3). These points are excluded from the fitting and the mean RM and B calculation but included in the plot to show the spike in RM, DM, and B-field when the pulsar is close to the Sun.

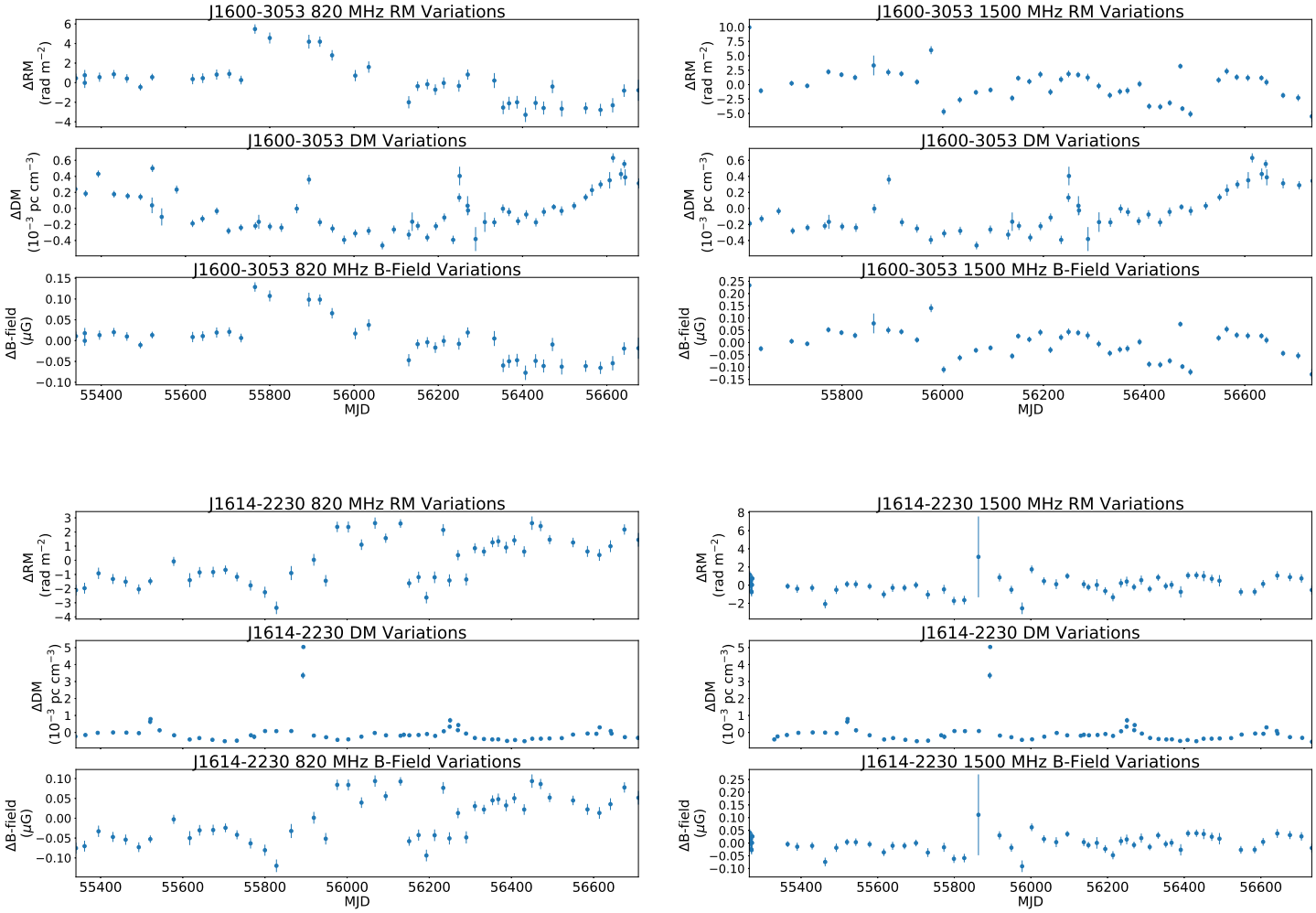

Figure 19. Ionosphere-corrected rotation measure, dispersion measure, and magnetic field changes over time for pulsars J1643–1224 and J1713+0747. The error bars on the RM are a combination of fitting for Faraday rotation and from the ionospheric correction, errors on the DM come from those on the DMX value, and errors on the magnetic field are a combination of the two. The trendline shown is that with the lowest reduced χ^2_r value of all of the trends. No trend is shown if the lowest χ^2_r value for the fits was that of a horizontal line with a slope of zero.

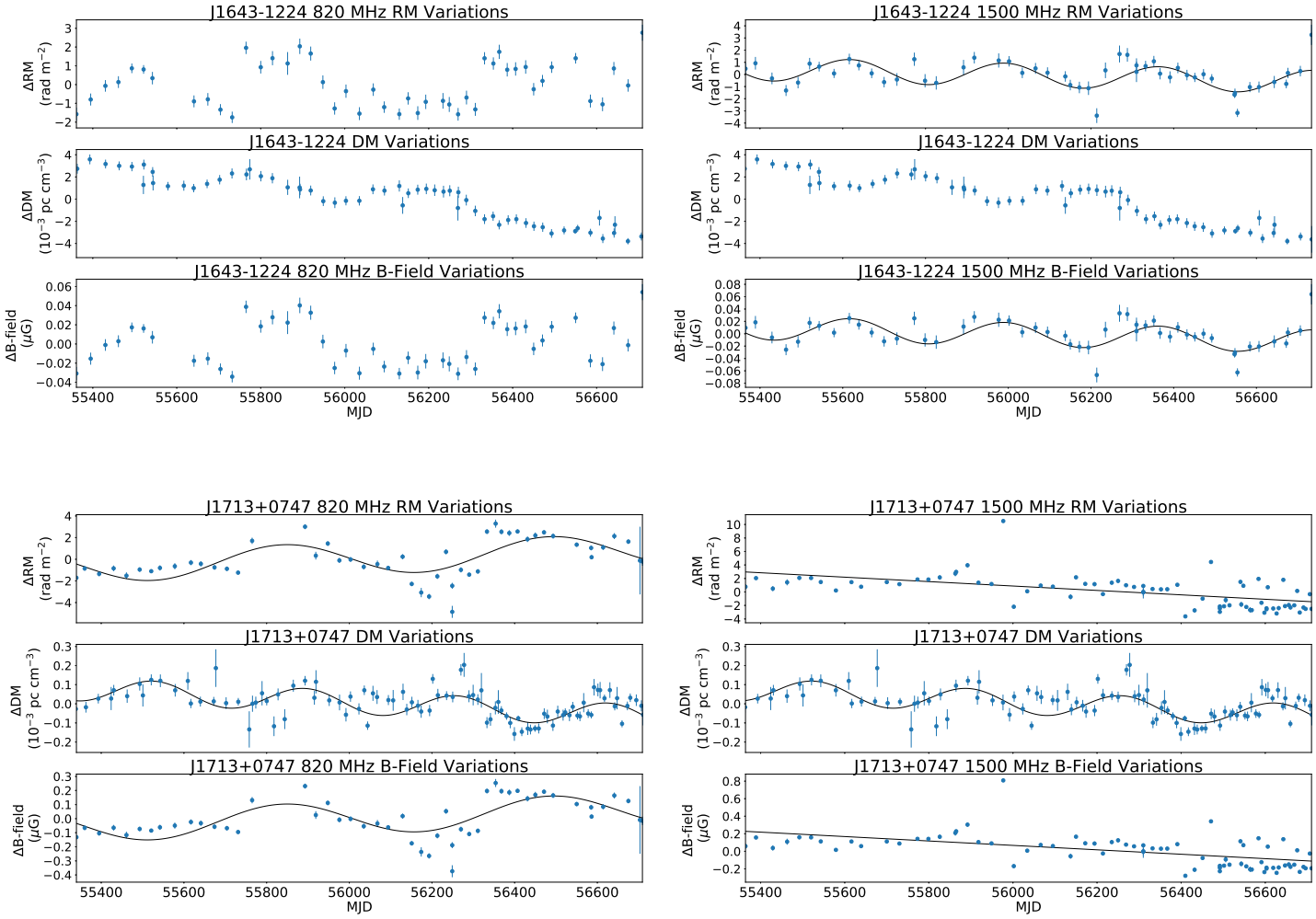

Figure 20. Ionosphere-corrected rotation measure, dispersion measure, and magnetic field changes over time for pulsars J1744–1134 and J1747–4036. The error bars on the RM are a combination of fitting for Faraday rotation and from the ionospheric correction, errors on the DM come from those on the DMX value, and errors on the magnetic field are a combination of the two. The trendline shown is that with the lowest reduced χ^2_r value of all of the trends. No trend is shown if the lowest χ^2_r value for the fits was that of a horizontal line with a slope of zero.

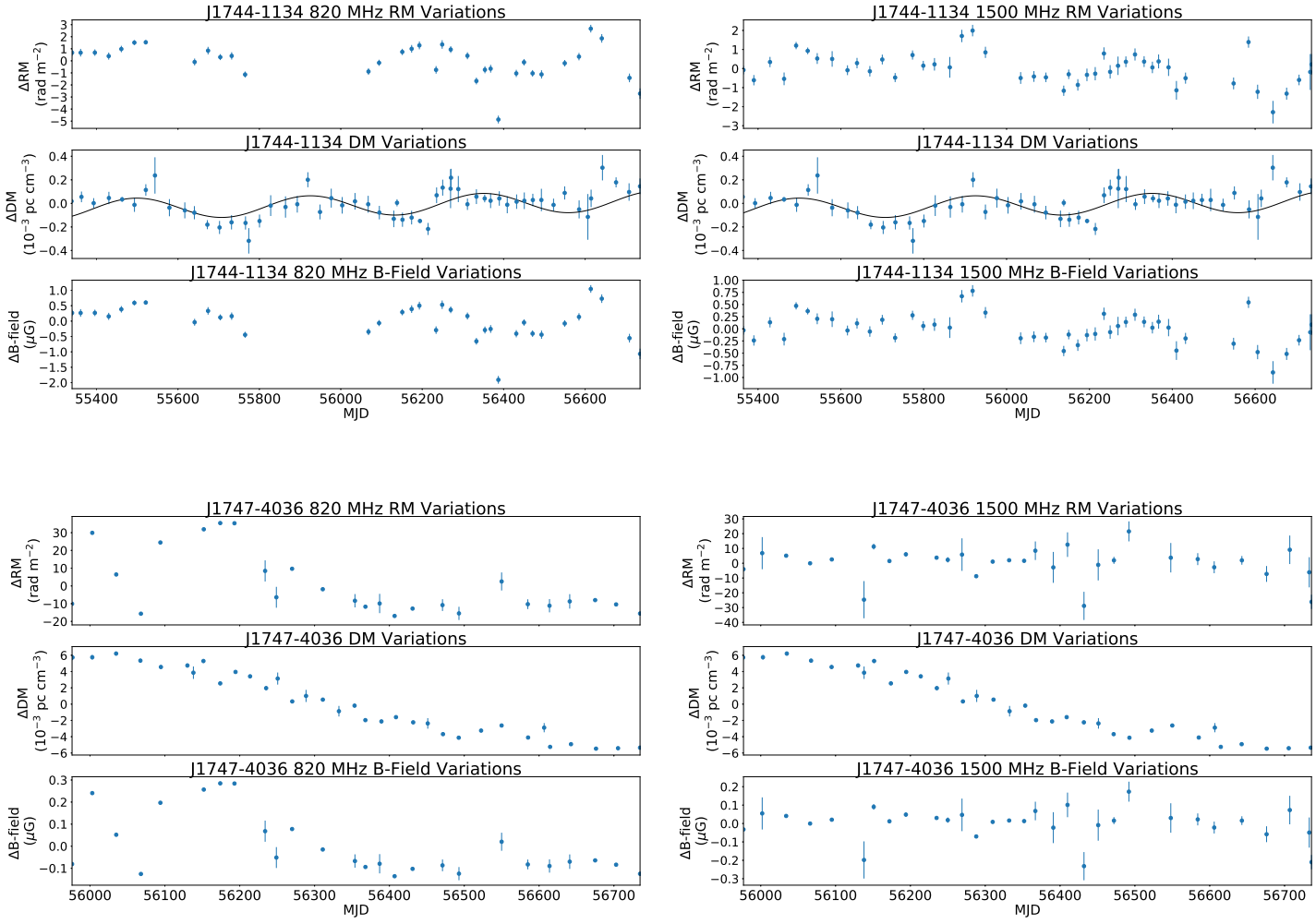

Figure 21. Ionosphere-corrected rotation measure, dispersion measure, and magnetic field changes over time for pulsars J1909–3744 and J1918–0642. The error bars on the RM are a combination of fitting for Faraday rotation and from the ionospheric correction, errors on the DM come from those on the DMX value, and errors on the magnetic field are a combination of the two. The trendline shown is that with the lowest reduced χ^2_r value of all of the trends. No trend is shown if the lowest χ^2_r value for the fits was that of a horizontal line with a slope of zero.

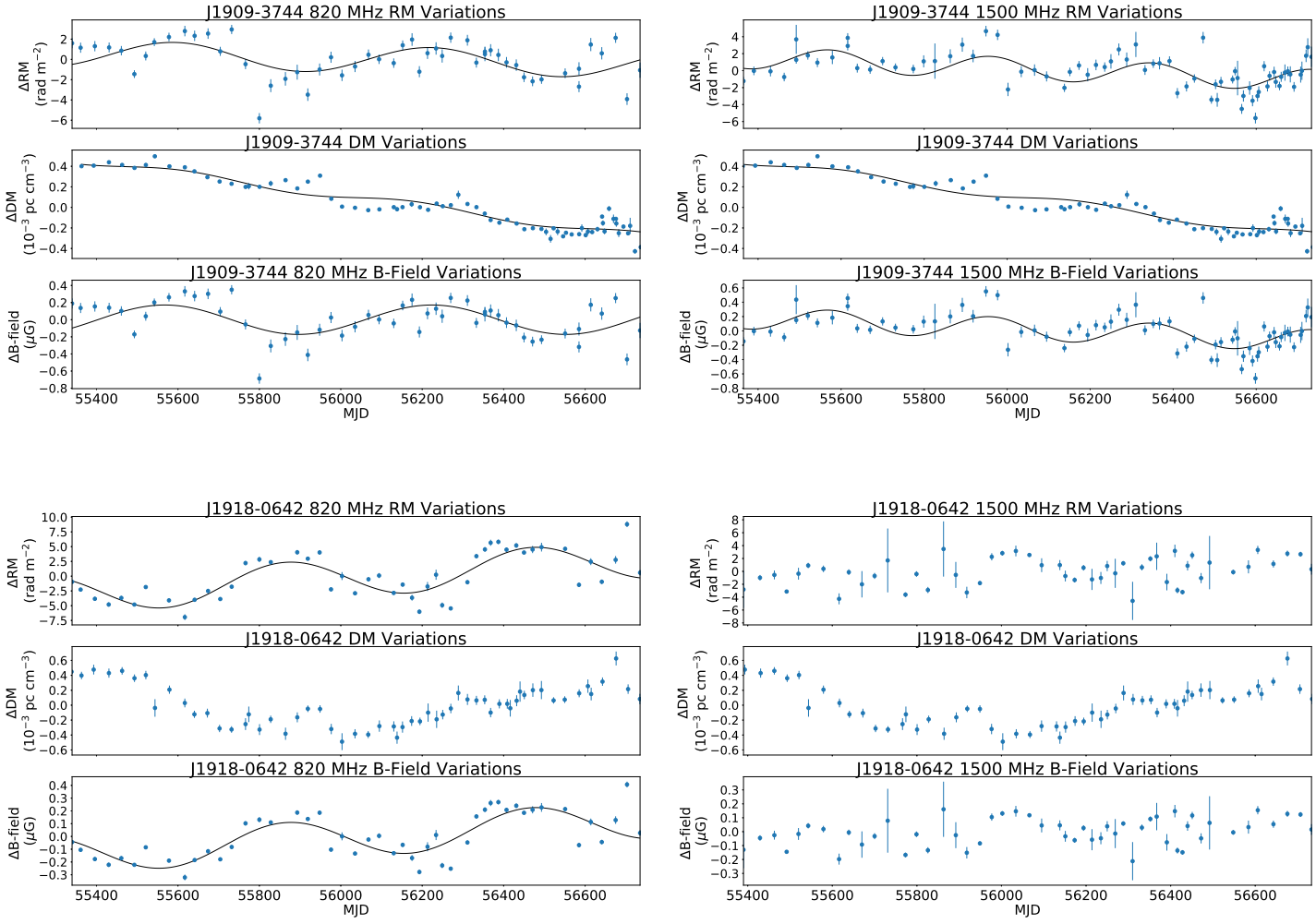

Figure 22. Ionosphere-corrected rotation measure, dispersion measure, and magnetic field changes over time for pulsars B1937+21 and J2010−1323. The error bars on the RM are a combination of fitting for Faraday rotation and from the ionospheric correction, errors on the DM come from those on the DMX value, and errors on the magnetic field are a combination of the two. The trendline shown is that with the lowest reduced χ^2_r value of all of the trends. No trend is shown if the lowest χ^2_r value for the fits was that of a horizontal line with a slope of zero.

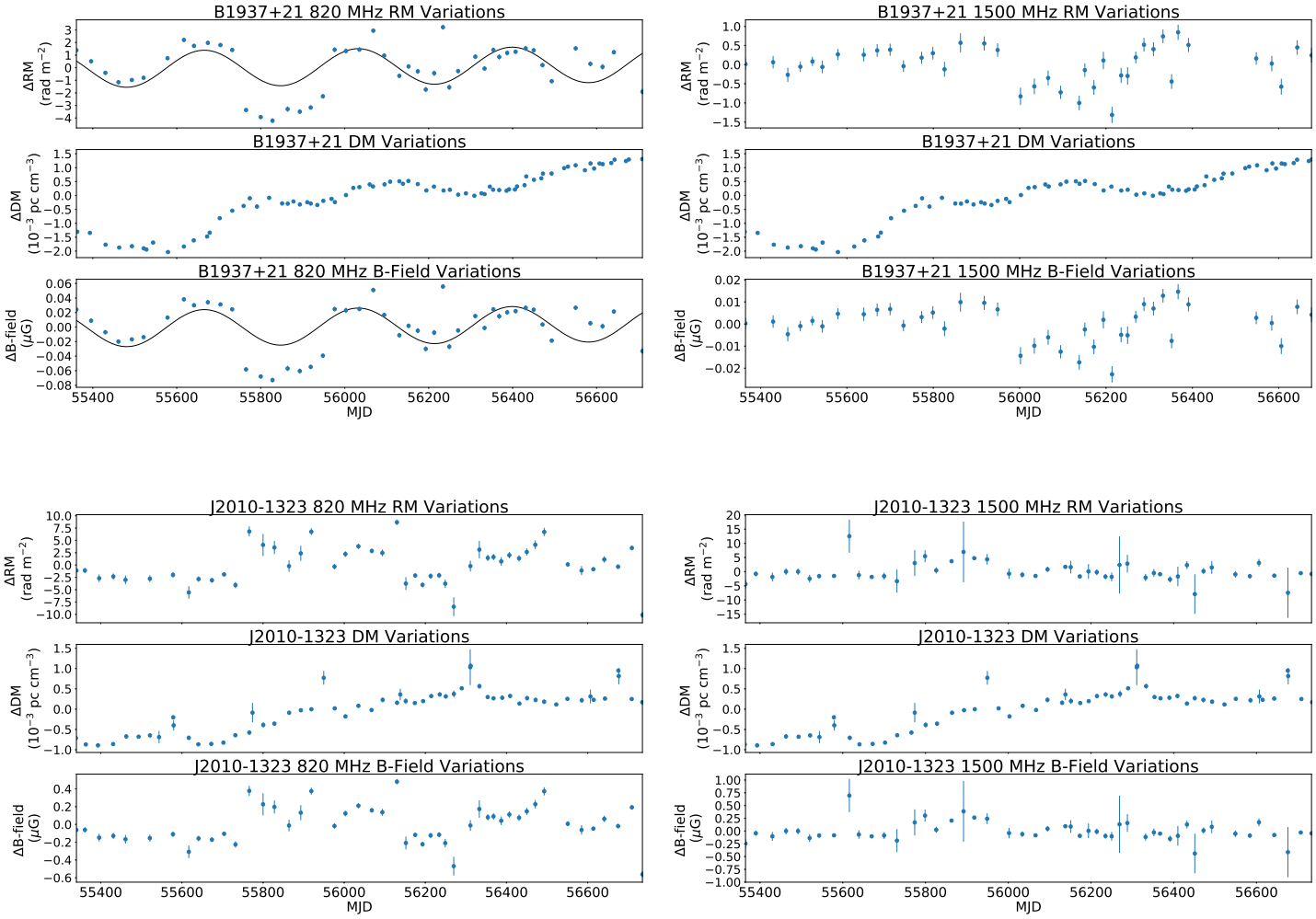

Figure 23. Ionosphere-corrected rotation measure, dispersion measure, and magnetic field changes over time for pulsars J2145–0750 and J2302+4442. The error bars on the RM are a combination of fitting for Faraday rotation and from the ionospheric correction, errors on the DM come from those on the DMX value, and errors on the magnetic field are a combination of the two. The trendline shown is that with the lowest reduced χ^2_r value of all of the trends. No trend is shown if the lowest χ^2_r value for the fits was that of a horizontal line with a slope of zero.

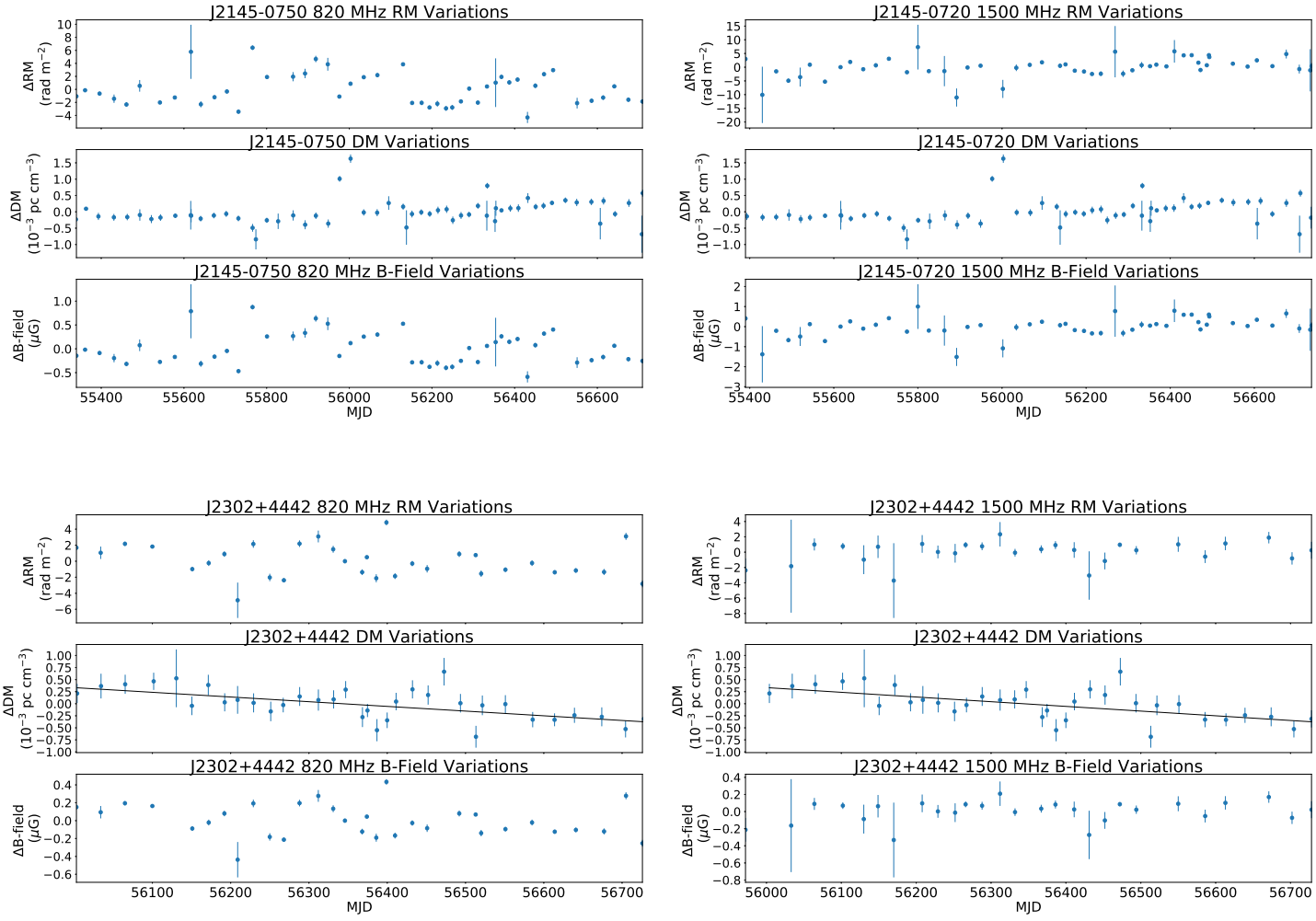

This figure "Orcid-ID.png" is available in "png" format from:

http://arxiv.org/ps/2104.05723v1